

AD _____

Award Number:
W81XWH-10-2-0101

TITLE :
Design, Fabrication, Characterization and Modeling of Integrated Functional Materials

PRINCIPAL INVESTIGATOR :
PI: Pritish Mukherjee, Ph. D.

CONTRACTING ORGANIZATION :
University of South Florida
Tampa, FL 33620, USA

REPORT DATE :
October , 2012

TYPE OF REPORT :
Annual

PREPARED FOR : U.S. Army Medical Research and Materiel Command
Fort Detrick, Maryland 21702-5012

DISTRIBUTION STATEMENT :

X Approved for public release; distribution unlimited

The views, opinions and/or findings contained in this report are those of the author(s) and should not be construed as an official Department of the Army position, policy or decision unless so designated by other documentation.

| REPORT DOCUMENTATION PAGE | | | Form Approved OMB No. 0704-0188 | | |
|---|------------------|--------------------------|--|--|---|
| Public reporting burden for this collection of information is estimated to average 1 hour per response, including the time for reviewing instructions, searching existing data sources, gathering and maintaining the data needed, and completing and reviewing this collection of information. Send comments regarding this burden estimate or any other aspect of this collection of information, including suggestions for reducing this burden to Department of Defense, Washington Headquarters Services, Directorate for Information Operations and Reports (0704-0188), 1215 Jefferson Davis Highway, Suite 1204, Arlington, VA 22202-4302. Respondents should be aware that notwithstanding any other provision of law, no person shall be subject to any penalty for failing to comply with a collection of information if it does not display a currently valid OMB control number. PLEASE DO NOT RETURN YOUR FORM TO THE ABOVE ADDRESS. | | | | | |
| 1. REPORT DATE (10-\$1-2012) | | 2. REPORT TYPE Annual | | 3. DATES COVERED (09-20-2011 to 09-19-2012) | |
| 4. TITLE AND SUBTITLE Design, Fabrication, Characterization and Modeling of Integrated Functional Materials | | | 5a. CONTRACT NUMBER | | |
| | | | 5b. GRANT NUMBER W81XWH--10-2-0101 | | |
| | | | 5c. PROGRAM ELEMENT NUMBER | | |
| 6. AUTHOR(S) PI: Pritish Mukherjee, Ph. D. co-PIs: Hariharan Srikanth, Ph.D.; Sarath Witanachchi, Ph. D.; George Nolas, Ph. D. pritish@usf.edu | | | 5d. PROJECT NUMBER | | |
| | | | 5e. TASK NUMBER | | |
| | | | 5f. WORK UNIT NUMBER | | |
| 7. PERFORMING ORGANIZATION NAME(S) AND ADDRESS(ES) University of South Florida Tampa, FL 33620, USA | | | 8. PERFORMING ORGANIZATION REPORT NUMBER | | |
| 9. SPONSORING / MONITORING AGENCY NAME(S) AND ADDRESS(ES) U.S. Army Medical Research and Materiel Command Fort Detrick, Maryland 21702-5012 | | | 10. SPONSOR/MONITOR'S ACRONYM(S) | | |
| | | | 11. SPONSOR/MONITOR'S REPORT NUMBER(S) | | |
| 12. DISTRIBUTION / AVAILABILITY STATEMENT Approved for public release; distribution unlimited | | | | | |
| 13. SUPPLEMENTARY NOTES | | | | | |
| 14. ABSTRACT The dynamically evolving needs of the U.S. soldier in the battlefield in response to changes in the technology of warfare and associated threats require advances in multiple areas including biomedical diagnostics, chemical sensing, communication technology, efficient power generation without increased payload, and mobile refrigeration. These technological advances are critically dependent on the development of new and currently non-existing materials. This research addresses the directed development of novel materials towards long-term needs of the United States Army. In order to address specific areas of integrated functional materials targeted towards the needs of the U.S. soldier in the field we have initiated research efforts in three main areas which are diagnostics and sensing, communication and energy, and power generation and refrigeration. The specific three independent "Tasks" that have been undertaken are: Task I: Nanostructured materials for biomedical diagnostics and chemical sensing Task II: Multifunctional composites for communication and energy applications Task III: Solid-state materials for power generation and refrigeration The specific outcome of the research activities is expected to lead to new devices/systems/composite materials useful for the USAMRMC. | | | | | |
| 15. SUBJECT TERMS Functional materials, integrated fabrication, nanobiotechnology, smart materials, multifunctional, dimensional integration, nanocomposites, sensor technology, thermoelectrics, solar cells, photovoltaics, polypeptide multilayer films | | | | | |
| 16. SECURITY CLASSIFICATION OF: | | | 17. LIMITATION OF ABSTRACT | 18. NUMBER OF PAGES | 19a. NAME OF RESPONSIBLE PERSON |
| a. REPORT U | b. ABSTRACT U | c. THIS PAGE U | UU | 55 | USAMRMC |
| | | | | | 19b. TELEPHONE NUMBER (include area code) |

Table of Contents

| | Page |
|--|-------------|
| | <hr/> |
| I. Introduction..... | 4 |
| II. Technical Description of Research Progress..... | 6 |
| III. Reportable Outcomes..... | 40 |
| IV. Conclusion..... | 45 |
| V. Bibliography..... | 53 |

Design, Fabrication, Characterization and Modeling of Integrated Functional Materials
(Program Director and PI: Prof. Pritish Mukherjee, Department of Physics, USF, Tampa, FL)
(co-PIs: Profs. Hariharan Srikanth, Sarath Witanachchi and George Nolas)

I. Introduction

The dynamically evolving needs of the U.S. soldier in the battlefield in response to changes in the technology of warfare and associated threats require advances in multiple areas including biomedical diagnostics, chemical sensing, communication technology, efficient power generation without increased payload, and mobile refrigeration. These technological advances are critically dependent on the development of new and currently non-existing materials. This research addresses the directed development of novel materials towards long-term needs of the United States Army.

Objective:

In addition to the integration of multiple functionalities with desirable properties (thermal, electrical, magnetic, mechanical, optical, etc.), the connection to real-world applications and devices also requires the seamless integration of dimensions (nano, micro, meso, macro) leading to integrated functional materials. We have initiated this Integrated Functional Materials Project at the Physics Department at the University of South Florida (USF) geared towards precisely addressing this grand challenge of dual integration. A series of targeted projects specifically address a spectrum of issues relevant to the needs of the U.S. soldier.

Specific Aims:

The Physics Department at the University of South Florida is home to a unique doctoral program in Applied Physics with an affiliated industrial practicum and nationally recognized research programs in physical and chemical materials synthesis and characterization of bulk materials, thin films and nanomaterials; crystal fiber growth; fundamentals of materials manufacturing processes and computational theoretical materials physics. This research synergistically coalesces existing expertise and leverages research infrastructure at USF in novel bulk materials synthesis, thin film growth, and nanotechnology. These goals are being further addressed through multidisciplinary research and new infrastructure development. The basic purpose of this project is to develop the novel science base both in the areas of multi-scale dimensional integration as well as multiple functional integration leading to previously unattained integrated functional materials.

Study Design:

In order to address specific areas of integrated functional materials targeted towards the needs of the U.S. soldier in the field we are directing the research efforts in three main areas which are diagnostics and sensing, communication and energy, and power generation and refrigeration. The specific three independent “Tasks”, further subdivided into seven “Projects” are:

Task I: Nanostructured materials for biomedical diagnostics and chemical sensing

(Technical Directors.: Drs. H. Srikanth and P. Mukherjee)

- Project 1* Functional magnetic fluids for biomedical applications
- Project 2* Nanoporous/nano-wire structures and polymer nanotemplates for sensing and molecular manipulation
- Project 3* Carbon-nanotube based sensors
- Project 4* Functional materials for affecting cell proliferation and locomotion

Task II: Multifunctional composites for communication and energy applications

(Technical Director: Dr. S. Witanachchi)

- Project 5* Tunable multifunctional nano- and heterostructures for RF and microwave applications
- Project 6* Flexible photonic materials for solar-based energy sources

Task III: Solid-state materials for power generation and refrigeration

(Technical Director: Dr. G. S. Nolas)

- Project 7* High-performance nanofabricated thermoelectric materials for power generation and refrigeration

II. Technical Description of Research Progress

The following discussion details the progress made on each of the Tasks during the fifth year of research (the second year of continuation funding):

Task I: Nanostructured materials for biomedical diagnostics and chemical sensing

The goal of this project is to synthesize and characterize advanced magnetic nanoparticles and nanocomposites for high-performance sensor and biomedical applications. During this year, we have successfully fabricated a variety of nanoparticles including FeCo, core/shell structured Fe/ γ -Fe₂O₃, FeO/Fe₃O₄, and NiFe₂O₄. Further, their structural and magnetic properties have been studied systematically. We have conducted MRI contrast enhancement effects of Fe/ γ -Fe₂O₃ nanoparticles using a pre-clinical scanner. The first study of the spin dynamics and probing exchange bias phenomena separately in the core and shell of Fe/ γ -Fe₂O₃ nanoparticles provided a new way for tailoring the material properties for practical applications. A graduate student Mr. Sayan Chandra received support and worked on this project during this quarter. In addition, graduate students Ms. Kristen Stojak and Mr. Jagannath Devkota, undergraduate student Mr. Ramon Ruiz, postdoctoral researcher Dr. Hafsa Khurshid and Research Assistant Professor Dr. Manh-Huong Phan were the key contributors to the project. A summary of our research activities and major results from the end of 2011 to 2012 is highlighted below:

Synthesis and characterization of Iron-Cobalt and core/shell Iron/Iron-oxide nanoparticles for MRI contrast enhancement

In this section, we will report the synthesis and characterization of an iron-cobalt alloy and iron/iron-oxide nanoparticles for clinical applications. Particles were synthesized by the high temperature reduction of organometallic compounds using oleic acid, oleylamine and tri-octyle phosphine as capping agents. The size and composition can be tuned by varying reaction parameters such as time, temperature, reacting chemicals and solution concentration. Pluronic triblock copolymer was used for the phase transformation of the particles' surface to obtain water dispersibility and biocompatibility. The hydrodynamic particle size was measured using a dynamic light scattering technique, which showed an average increase of 20 nm in the particle size after surface functionalization. In-vitro T₂ contrast studies were performed using a 7 Tesla Agilent ASR 310 MRI scanner. Changes in T₂-contrast are evident in the T₂-weighted image, and show the potential utility of these nanoparticles as negative contrast agents.

Magnetic nanoparticles that are surface functionalized with biomolecules have shown promise for clinical applications such as, imaging, use as biomarkers, use as biosensors, and targeted drug delivery [1]. For clinical trials, all of these applications rely on the magnetization of nanoparticles used [2], so an important challenge is to synthesize nanoparticles with high magnetic moments, so as to limit the quantity to be used in the body [3]. Iron and iron-cobalt alloy nanoparticles exhibit much higher magnetic moments than those of iron-oxide of comparable size, due to intrinsic magnetic properties.

Recently, there have been some reports about the synthesis and functionalization of iron-cobalt and iron nanoparticles with high magnetic moments [4]; however, not much attention is paid to controlling the size and shape of these nanoparticles during synthesis. The nanoparticle's shape plays an important role in the control of magnetic properties such as coercivity (H_C). The control of particle size and shape in nanoparticle systems such as iron and iron-cobalt is still an important challenge. In this work, nanocubes of an iron-cobalt alloy with controlled size and composition have been synthesized using high temperature reduction of organometallic compounds. In order to achieve biocompatibility and water dispersibility, pluronic-F127 (PEO-PPO-PEO) triblock copolymer was used for surface modification of nanoparticles via physical adsorption.

Experimental details

Iron-cobalt alloy (FeCo) nanoparticles have been synthesized by thermally decomposing iron-III-acetylacetonate (Fe-acac), cobalt-III-acetylacetonate (Co-acac), and 1-octadecene in the presence of oleic acid (OA) and oleylamine (OY) surfactants at 300°C. In a typical synthesis procedure, 6 mmols each of Fe-acac and Co-acac were dissolved in 20 ml of 1-octadecene, in the presence of 6 mmols each of OA and OY at 100°C while degassing with Ar+H₂(5%). The mixture was heated to 300°C and allowed to reflux for 2 hours under a controlled flow of Ar+H₂ (5%). Afterwards, the reaction mixture was cooled to room temperature by removing the heating mantle and precipitated by adding 50 ml of ethanol. Byproducts and surfactants were removed by centrifuging at 7000 rpm in the presence of ethanol. The resulting FeCo alloy nanoparticles were then dispersed in hexane. Iron nanoparticles were synthesized by thermally decomposing iron-pentacarbonyl in octadecene, oleic acid and oleylamine as has been described in our previous reports [10]. Particles were surface modified (phase transferred) with pluronic (F127) which is known to be physically adsorbed at the particle's surface. When possible, the phase transformation was done in a nitrogen atmosphere and extreme care was taken to avoid oxidation. The mass ratio for particles to pluronic was kept to 1:10. About one gram of pluronic was used for 1ml of the nanoparticle-hexane solution (concentration 5mg/ml). F127 was dissolved in 20 ml DI water at room temperature and then mixed with particles in solution via mechanical shaking for six hours. Afterwards, hexane was evaporated in a desiccator and particles were centrifuged to get rid of extra F127 and precipitated down. The phase transformed particles were dissolved in water.

Results and Discussion

Fig. 1 shows the X-ray diffraction (XRD) pattern of FeCo nanoparticles taken from dry particles on a silicon substrate. Strong FeCo reflections of (110), (200) and (211) planes were observed. No reflections were observed from Co, Fe and their oxides. The grain (crystalline) size was calculated to be 20 nm from XRD using Scherrer's formula ($0.9\lambda/\beta\cos\theta$). Separately, the particle size was determined from transmission electron microscopy (TEM) micrographs by counting more than 200 particles. Fig. 2 shows a TEM image of the OA- and OY-capped FeCo nanoparticles. Particles show a clear cubic shape with an average size 20 ± 1.5 nm. The close correspondence between particle size determined from TEM and calculated from XRD indicates that particles are single crystalline. Further high-resolution TEM (HRTEM) images also reveal the single crystal structure in these nanoparticles (Figure 2b). Elemental analysis using energy dispersive X-ray (EDX) spectroscopy revealed that particles are composed of 52 % atomic Fe and 48 % atomic Co.

It is seen that when OY was replaced with trioctyl phosphine (TOP) during synthesis, while keeping the molar concentration the same, the average particle size was reduced to 15 nm, while a broad particle size distribution was introduced (Fig. 3). These results are identical to what Peng et al. [6] previously reported with their FeCo nanoparticle synthesis. In addition, particle shape also became non-uniform with a predominantly spherical shape. It is well known from literature that the nucleation rate plays a very important role in obtaining particles of a uniform shape and size.

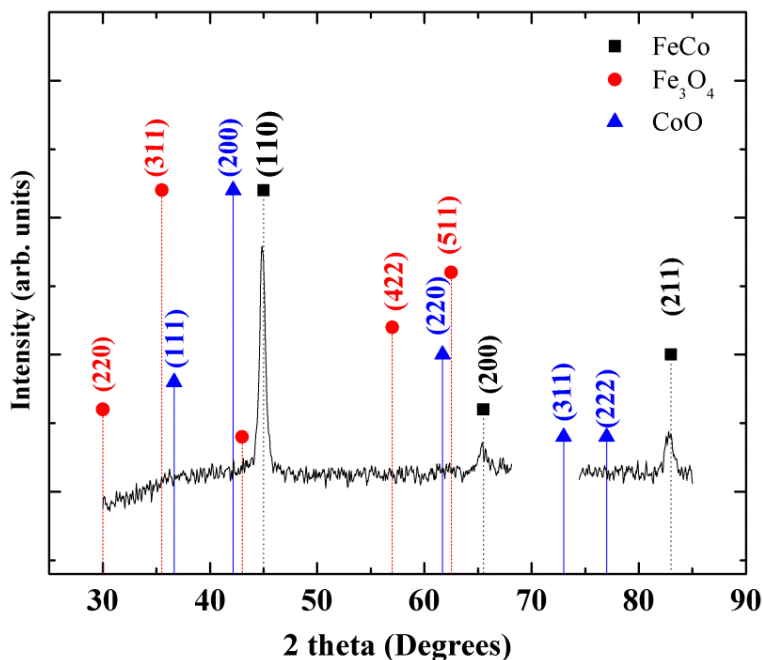


Figure 1: XRD pattern of nanoparticles corresponding to FeCo alloy crystal structure without any oxide phases present. The scan at 2 theta = 68-73° is removed to avoid the sharp peak from the Si substrate at 2 theta = 69°.

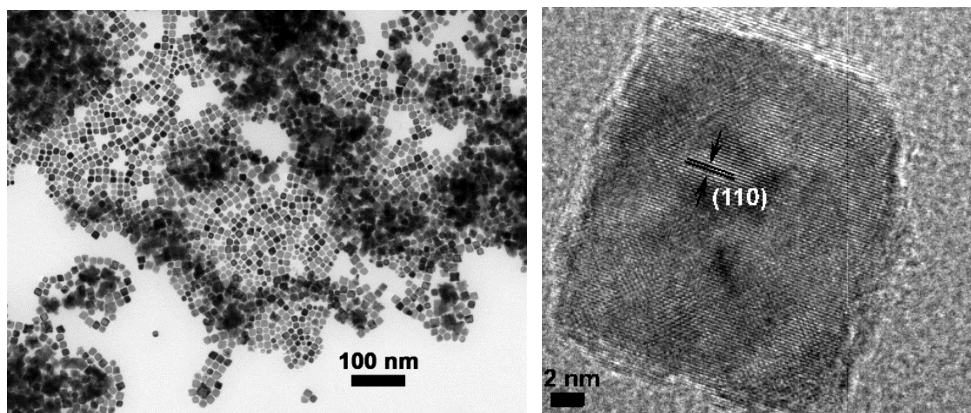


Figure 2: (a) Bright Field TEM image of FeCo nanoparticles, capped with OA and OY and (b) HRTEM of one the particles.

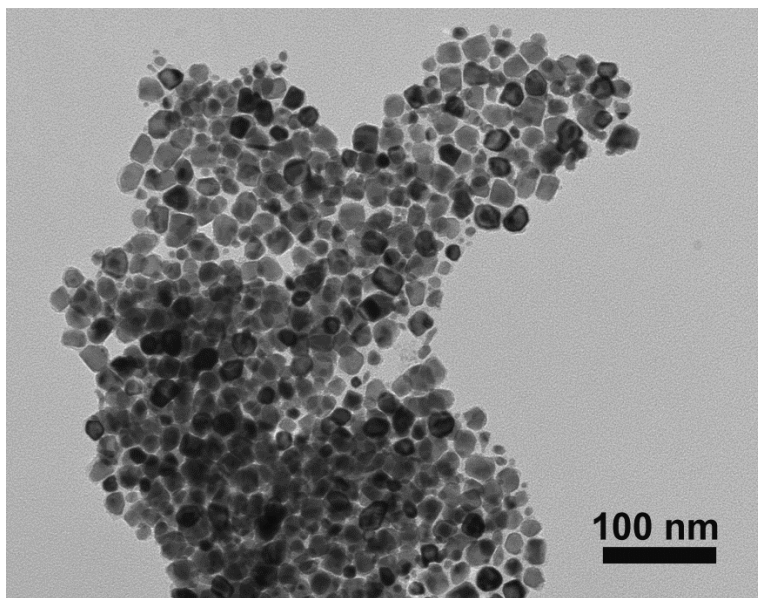


Figure 3: Bright field TEM image of TOP capped particles.

temperature measured for the OY and TOP capped particles. The OY capped particles have a room temperature magnetization above 160 emu/g where as TOP capped particles show a room temperature magnetization of 120 emu/g. This effect could be due to the presence of small nanoparticles, which are in the superparamagnetic regime. This is further evidenced by the reduced coercivity in TOP capped particles, when compared to OY capped particles. The non-collinearity of magnetic moments on the particles' surface, combined with spin canting, could have caused a lower magnetic moment in the case of small particles [7]. It is worth mentioning that this value is estimated without correction for the surfactant present at the surface of the particles. The iron nanoparticles were synthesized by the thermal decomposition in an inert atmosphere in the presence of OA and OY [5]. These particles exhibit a core/shell morphology where core is single crystalline bcc iron and shell is composed of randomly oriented iron oxide crystallites (Fig. 5).

A single rapid nucleation event favors particle growth with a uniform size and shape, whereas in the case of a slower nucleation rate, reactants are unevenly depleted from solution, leading to variations in growth rate for seeds formed at different times. It is likely that the use of TOP slows the nucleation rate and hence, both particle size and shape appeared non-uniform. Particle composition also varies from 52% to 60% atomic Fe (with 48% to 40 % atomic Co) when OY is replaced with TOP, as concluded from the EDX analysis.

Fig. 4 shows typical hysteresis curves at room

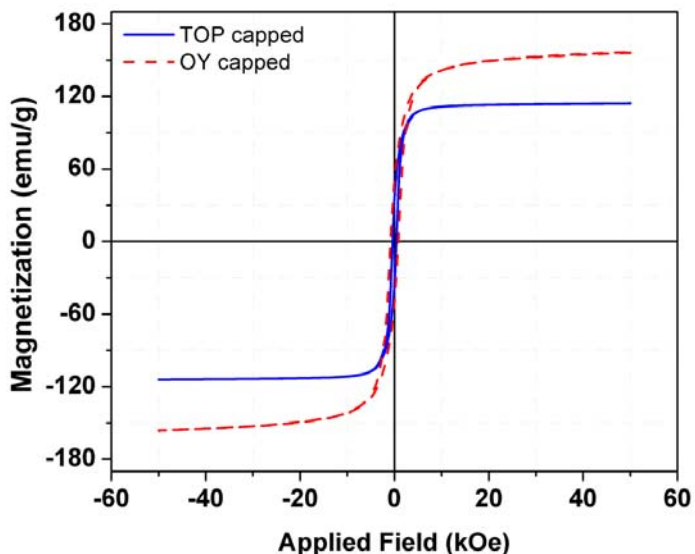


Figure 4: Hysteresis curves for OY and TOP-capped FeCo particles.

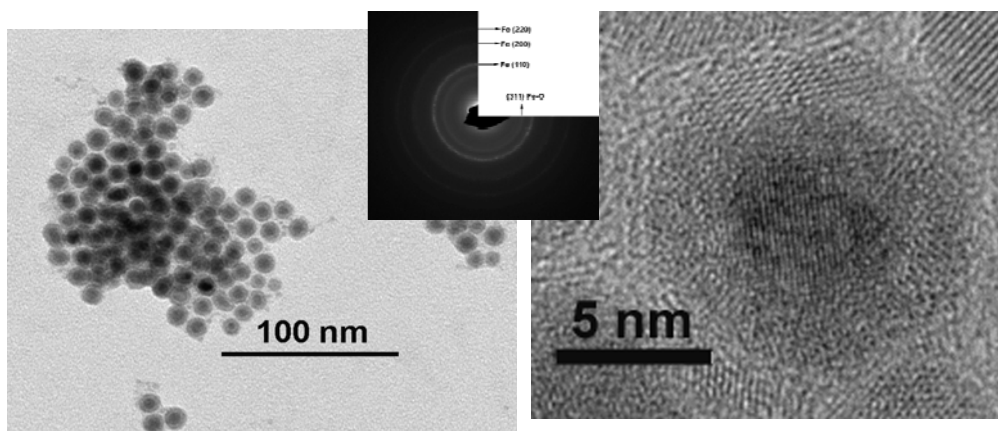


Figure 5: TEM imaging of core/shell structured iron/iron-oxide nanoparticles.

The hydrocarbon chains from OA and OY make these OA/OY coated particles hydrophobic and they are soluble only in nonpolar or weakly polar solvents via steric repulsions [3]. However, for biomedical applications, these particles must be water dispersible and stable under various conditions, such as at pH ranging from 5-9, under salt concentrations of up to a few hundred mmol/L and at temperatures up to 95°C. This can be achieved by surface functionalization (phase transformation) of hydrophobic nanoparticles by depositing hydrophilic agents (polymers, surfactants) at the particle's surface or by ligand exchange. In the first approach, a double layer structure forms over the surface of nanoparticles due to hydrophobic interaction between hydrocarbon chains, and immobilizes the new ligand with a functional group over the original surfactant shell [2]. Such kind of surface functionalized particles can be dispersed in various solvents, depending upon the functional group of modifying ligand. A common example of such a ligand is pluronic (F-127) copolymer [8]. In the second approach, strong chemical interactions between the nanoparticle surface and modifying ligand causes the replacement of the original surfactant (OA, in our case) with the newly added one (F-127, in our case). The functional group at the other end of the ligand provides water dispersibility via electrostatic repulsion. F-127 is known to reduce the adsorption of proteins and adhesion of cells onto surfaces, and hence increase biocompatibility and solubility of hydrophobic drugs. It is made from two chains of polyethylene oxide (PEO) and one chain of polypropylene oxide (PPO) in an PEO-PPO-PEO PEO-PPO-PEO triblock copolymer configuration. Previously F-127 has been reported to obtain water dispersibility of magnetite nanoparticles.

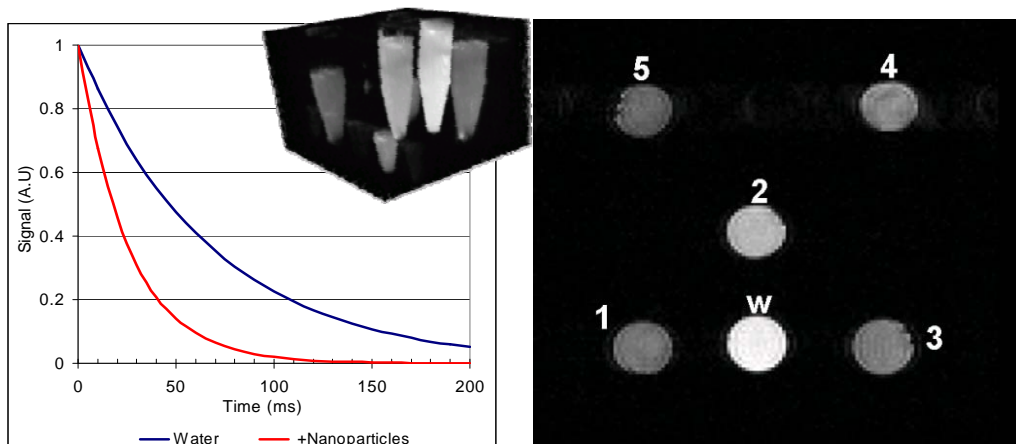


Figure 6: Theoretical nanoparticle induced negative contrast (left panel); T_2 -weighted phantom image displaying negative contrast agent concentration dependence of transverse relaxation (right panel). The concentration of particles in each tube is $1 = 20 \mu\text{g/ml}$, $2 = 10 \mu\text{g/ml}$, $3 = 25 \mu\text{g/ml}$, $4 = 42 \mu\text{g/ml}$, $5 = 55 \mu\text{g/ml}$, $W = 0 \mu\text{g/ml}$ (water only).

Figure 6 (left) shows relative signal intensity due to presence of nanoparticles, modifying the T_2 relaxation. The blue line represents the T_2 relaxation of water, while the red line represents the T_2 relaxation in the presence of nanoparticles. The proximity of such nanoparticles to water molecules shortens the T_2 relaxation of water protons, yielding lower intensity over the relaxation time. Core/shell structured Fe/ γ -Fe₂O₃ nanoparticles of average size 10.2 ± 1.5 nm were used for T_2 -Weighted MR Imaging (Fast Spin Echo), with TR = 3196 ms, and TE = 8.31 ms using a 7 Tesla Pre-clinical MRI scanner.

In summary, we have successfully synthesized shape-controlled FeCo nanoparticles possessing high magnetic moment by thermally decomposing Fe-acac and Co-acc without any partial oxidation. Core/shell structured iron/iron-oxide nanoparticles were also synthesized by the thermal decomposition of iron pentacarbonyl. The water dispersibility and biocompatibility of the oleate coated particles can be obtained via surface modification with F-127, which is known to be adsorbed at the particles' surface via Vander Waals interactions between the aliphatic chain of (OA) and the hydrophobic part (PPO) of pluronic. Measurements of the transverse relaxation time T_2 of the core/shell structured iron/iron-oxide nanoparticle solution at 7 Tesla with varying concentration confirms that these particles are an excellent T_2 contrast agent for MRI. Future work would be focused on obtaining superparamagnetic FeCo nanoparticles and studying their MRI contrast enhancement properties.

Mechanism and controlled growth of shape- and size-variant core/shell FeO/Fe₃O₄ nanoparticles

In this section, the shape and size controlled synthesis of core/shell structure wüstite/magnetite (FeO/Fe₃O₄) nanoparticles by solution phase chemical reaction are presented. The molar ratios and concentrations of surfactant are found to be key parameters in controlling particle size. Twinning and crystal defects can be introduced during the early stage of a reaction, which forms triangular nanoplates, or faceted rods of Fe₃O₄, depending upon the number of twin boundaries in the seed. Particles can be partially oxidized to form core/shell structured FeO/Fe₃O₄, or fully oxidized to form Fe₃O₄ as evidenced by transmission electron microscopy (TEM), X-ray diffraction (XRD) analysis and magnetic data. This synthesis technique is found to be the most promising method to synthesize shape- and size-variant core/shell FeO/Fe₃O₄ (by partially oxidizing FeO) or to obtain shape- and size-variant Fe₃O₄ nanoparticles.

Over the past few decades, iron oxide nanoparticles have been widely explored because of their potential applications in various fields, including storage media, environmental remediation, and as multifunctional clinical tools. However, recently much attention has been paid to wüstite (FeO) nanoparticles because of their interesting defect-related magnetic properties and their ability to transform to different phases of nanostructures when processed chemically or thermally [9]. At room temperature, the formation of FeO is only possible at the nanoscale due to the large contribution of surface energy in nanoscale materials. In order to attain stability of FeO nanoparticles, one possible approach is to manipulate surface energy contribution by varying the size and shape of the nanoparticles. It is well-known that different shapes of nanoparticles can introduce electronic and optical properties that are different from those observed in their spherical counterparts. Furthermore, nanoparticle's shape plays an important role in determining magnetic properties. Because of higher symmetry of the fcc crystal structure for iron oxide crystals, isotropic morphologies (spheres, octahedrons, cuboctahedrons) are much easier to synthesize. In order to synthesize anisotropic morphologies (eg. octopods and rods), the seed structure must be manipulated by varying the free energy of the crystal lattice. In this work, we report a systematic study of the shape and size control of FeO nanoparticles by varying parameters in the chemical reaction. Furthermore, we aim to investigate the exchange coupling phenomena in core/shell structured FeO/Fe₃O₄ nanoparticles. Our findings give direct evidence that during the initial stage of FeO nanoparticle formation, the seeds adopt a cuboctahedral morphology (wolf theorem). In the growth step, competitive growth rates of {111} and {100} facets can be used to tune the final shape of these nanoparticles. This is of practical importance, as such nanostructures can be ideal for use in applications where their anisotropic magnetic properties can be controlled using an “exchange bias” mechanism.

Experimental details

Particles are synthesized by high temperature reduction of iron-organometallic salt in an inert atmosphere. Thermally unstable Fe-acac starts decomposing around 100–105 °C to produce carbon dioxide and acetone [10]. Synthesis of various Fe-based nanoparticles has been reported previously using this decomposition reaction. In a typical synthesis, 0.75 mmol Fe-acac was dissolved in 20 ml octadecene, in the presence of 5 mmol OA and 5 mmol OY. The mixture was purged with Ar at an elevated temperature of ~100°C, to get rid of free oxygen released from the solution. The temperature was raised to 200°C, where the solution reacted for one hour. The

mixture color was changed from dark red to black indicating the decomposition Fe-acac. Afterwards, the mixture was further heated to 300°C at a rate of 10°C per minute and refluxed at 300°C for one hour. The heating source was then removed and the reaction mixture was allowed to cool down. It is worth to mentioning that Ar was continuously flowed during the reaction. The system was opened after adding ethanol and then was centrifuged to obtain a black product that was precipitated. The supernatant was discarded and the black product was then dispersed in hexane (20 ml).

Results and Discussion

Figure 7 shows TEM images of all the shapes obtained in this work along with selected area diffraction pattern from area shown in Figure 7(a) with different reaction conditions used for synthesis of nanoparticles with different shapes. Depending upon the reaction conditions, particles adopt a cubic, spherical, octopodal, triangular, rod or cuboctahedral shape. When the OA/OY ratio decreases from 1 (so that there is more OY than OA in the system), particles' shape varies from cubic to spherical. Additionally, when 1,2-hexadecanediol was added to the reaction mixture with a concentration of 15 mmol, while keeping the OA/OY ratio to 1, cuboctahedral shaped particles were observed. The use of surfactants as a reaction solvent together with changing the OY/OA molar ratio were found to be another way to control particles' shape. With an OA/OY ratio of 0.4, particles have spherical shape. When this ratio was increased to 1, while fixing all the other parameters, the resulting particles had an octopodal shape. Furthermore, the formation of octopods was also observed when the solvent concentration was reduced to half, and also when the precursor and surfactant concentration was doubled. Another reaction parameter that was studied was the precursor decomposition time, which was varied from 10°C/min to 2°C/min in order to control the reaction kinetically instead of thermodynamically. A slower reaction rate appeared to favor the formation of rods and triangular particles.

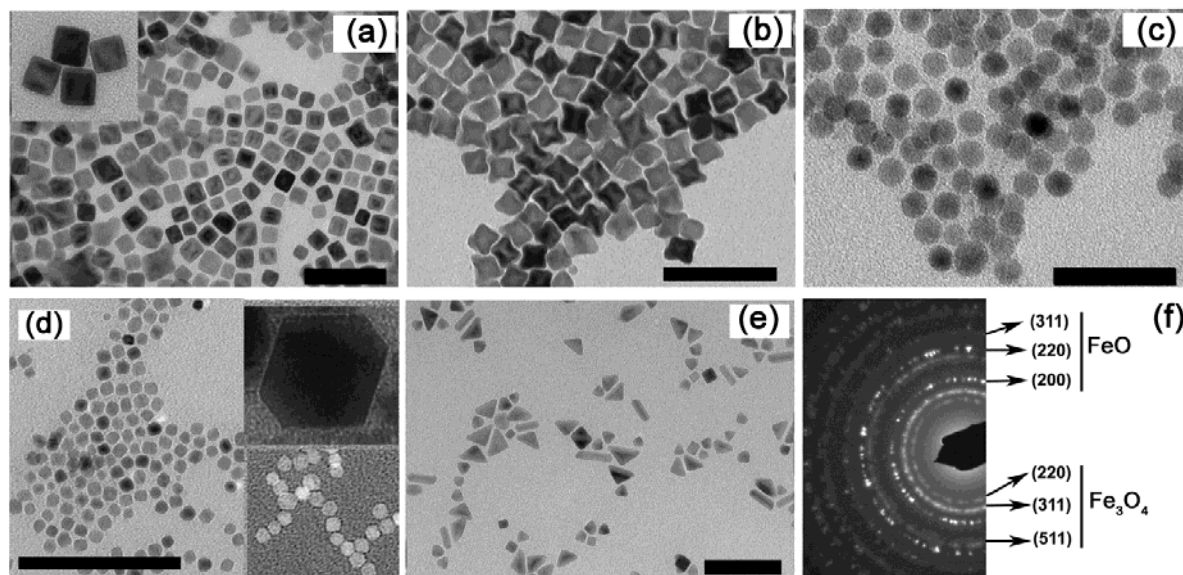


Figure 7: Formation of cubical (a), octopod-cubic (b), spherical (c), octahedral/cuboctahedral (d), triangular/hexagonal nanoplates and faceted rods/beams shape nanoparticles (e) and the selected diffraction from cubic particles (f). The inset of (a) and (d) shows zoom-in view of cubes and octahedrons. The scale bar is 100 nm.

The composition and crystallographic phase of nanoparticles was studied from their XRD and selected area diffraction (SAD) analysis. Figure 8 (upper panel) shows the XRD plot of cubic nanoparticles. It can be seen that all peaks correspond to the characteristic reflections of the wustite phase of iron oxide (FeO JCPDF #46-1312), FeO, with the same intensity ratios as its bulk powder counterpart. The XRD micrographs for octopods and spheres also showed a similar crystallographic structure, with the exception of estimated grain size. The grain sizes were calculated from XRD using Sherrer's formula for cubes (20 nm), octopods (25 nm) and spheres (16 nm) and match well to the sizes obtained from TEM, indicating that each particle is single crystalline in nature. When the XRD data of the various nanoparticle samples were analyzed, it was deconvoluted into its constituents using an X-Fit program (a graphical X-ray line profile fitting program XFIT that integrates the familiar Pseudo Voigt and Split Pearson functions). It is observed that all prominent x-ray peaks are the peaks from FeO (Figure 8 (lower panel)). However, there is a broad peak at 2-theta $\sim 35.5^\circ$ that appears as a shoulder, superimposed on the sharp crystalline FeO (111) peak; this indicates the presence of Fe₃O₄. It is most likely that the particle's surface started oxidizing to Fe₃O₄ giving rise to a core/shell type morphology, due to the metastability of FeO at room temperature.

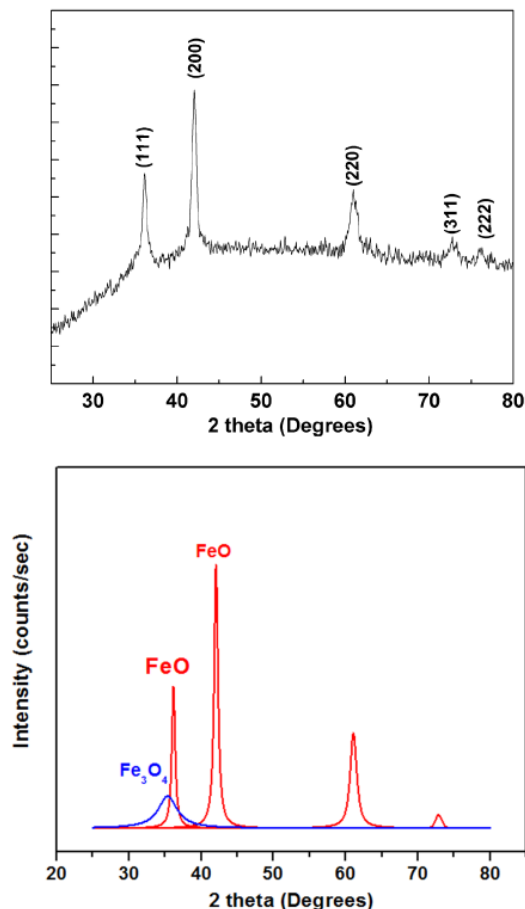


Figure 8: (upper panel) XRD micrograph of FeO nanoparticles and (lower panel) deconvoluted parts of the fitted curve.

We have also carried out HRTEM studies on different shapes of FeO nanoparticles to determine the crystallinity, homogeneity and facet orientations. The HRTEM studies of the cubic nanoparticles revealed their single crystalline nature as the lattice fringes continued uninterrupted throughout the nanoparticle. Additional information about the structure and composition of the nanocubes can be obtained through detailed analysis of HRTEM images. HRTEM image (Figure 9) of a nanocube along [001] zone axis along with corresponding fast Fourier transform (FFT) shows that cubic particles are bounded by {100} facets with some {110} truncation at the corners. The distance between lattice fringes is measured to be 0.208 nm which corresponds to (200) FeO. It is worth mentioning that this distance (0.208 nm) is close to the (400) lattice planes of Fe₃O₄. The main direction $\langle 100 \rangle$ is indicated on the image (Figure 9), as well as the measured inter planar distance of 2.98 Å, which is identified as the separation between (220) planes in magnetite. The particles exhibit core/shell-type morphology with FeO as the core and Fe₃O₄ as

the shell, according to XRD data. In the case of spherical particles with a core/shell-type morphology, the inner contrast variation is more pronounced. The selected area diffraction (SAD) pattern from these spherical particles is shown in Figure 7(f) and indicates that all diffraction rings correspond to the characteristic reflection from FeO and Fe₃O₄ reflection. It is very clear that the diffraction rings from Fe₃O₄ are broad and uniform whereas diffraction rings from FeO are bright and sharp. This is due to the difference in grain size of the two phases. Since we did not see indication of bimodal size distribution, the broader reflections from Fe₃O₄ must be from the shell of the nanoparticles. It should be noted that HRTEM imaging does not allow us to distinguish between the core and the shell in this system, because the shell grows epitaxially over the core, and the crystal structure of FeO and Fe₃O₄ are similar.

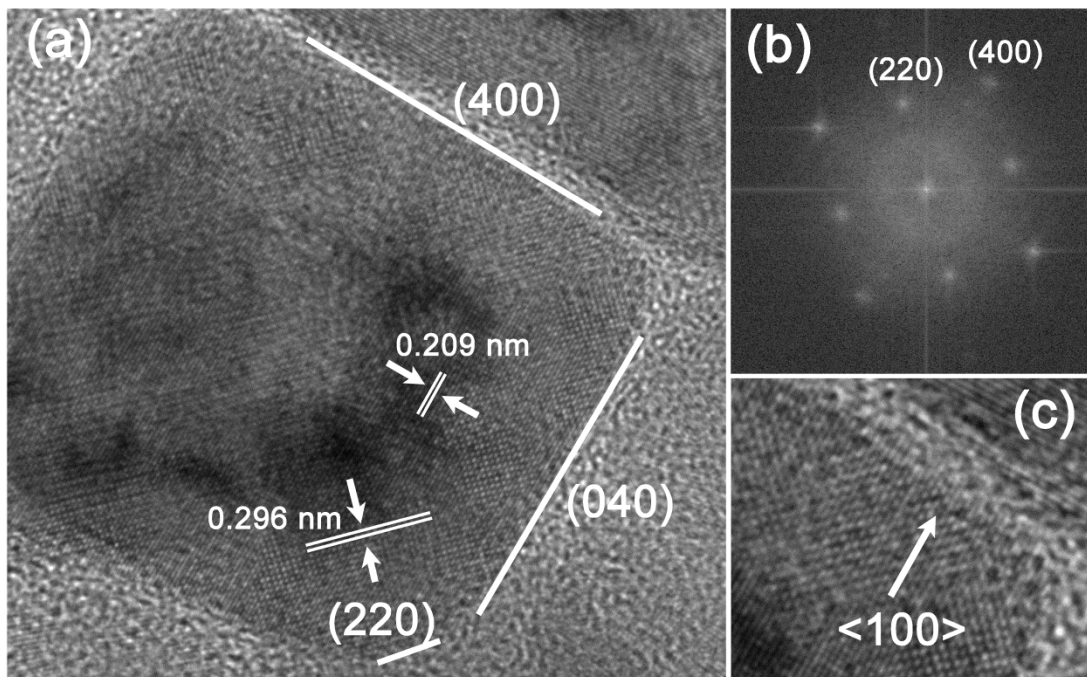


Figure 9: HRTEM of cubic nanoparticles (a) and the corresponding FFT (b). The arrow indicates $\langle 100 \rangle$ direction in (c).

In summary, we have successfully reported a novel chemical reaction route for the synthesis of core/shell structured FeO/Fe₃O₄ nanoparticles with controlled size and shape by varying reaction conditions. It is found that particles can grow in either isotropic or anisotropic shapes depending upon the reaction kinematics and thermodynamics. Our results demonstrate a correlation between a particle's shape and the reduction mechanism (kinetic or thermodynamic) in the case of FeO/Fe₃O₄ core/shell nanoparticles and Fe₃O₄ nanoparticles. Particles can be oxidized chemically or thermally to form inverse spinel Fe₃O₄ nanoparticles. Following the same chemical technique, it is possible to synthesize rods and triangles of Fe₃O₄ by introducing twinings and defects in the crystal structure of the seed. In order to create a plate-like structure, the reaction was controlled kinetically by slowing the decomposition rate. One tantalizing aspect of our results is that the charge ordered Verwey transition associated with Fe₃O₄ was seen in all FeO/Fe₃O₄ particles, independent of size and shape. Particles show strong exchange coupling (exchange bias field ~ 5 kOe) when cooled to 5K under a magnetic field of 50 kOe caused by interfaces between antiferromagnetic FeO and the ferrimagnetic Fe₃O₄ leading to horizontally and vertically shifted hysteresis loops and enhanced coercivity. This synthesis process can be

regarded as an efficient way to fabricate a series of different isotropically and anisotropically grown iron-oxide nanoparticles for a variety of applications.

Spin dynamics of core-shell Fe/ γ -Fe₂O₃ nanoparticles

The system in this present study is ~ 10 nm Fe/ γ -Fe₂O₃ nanoparticles synthesized by a thermal decomposition technique. We have investigated the magnetization dynamics by performing static and dynamic magnetic measurements.

The core-shell structured nanoparticles were prepared by high temperature reduction of iron pentacarbonyl (Fe(CO)₅) in octadecene in the presence of OY and TOP, details of which have been published [11]. Briefly, OY and TOP (molar ratio 1:1) were dissolved in octadecene in a three necked flask and heated in an airtight atmosphere while continuously purging with Ar+5%H₂ to eliminate any free oxygen dissolved in the solvent and surfactants. Fe(CO)₅ was injected at 220°C and refluxed for one hour to yield a dark solution. The nanoparticles were precipitated and extracted by adding an absolute ethanol to the reacted solution, followed by centrifuging. Structural and microstructural studies were performed using JEOL JEM 3010 FX TEM. The magnetic properties were carried out using a Quantum Design Physical Properties Measurement System (PPMS) with a VSM option over a temperature range of 5 – 300 K and applied fields up to 50 kOe.

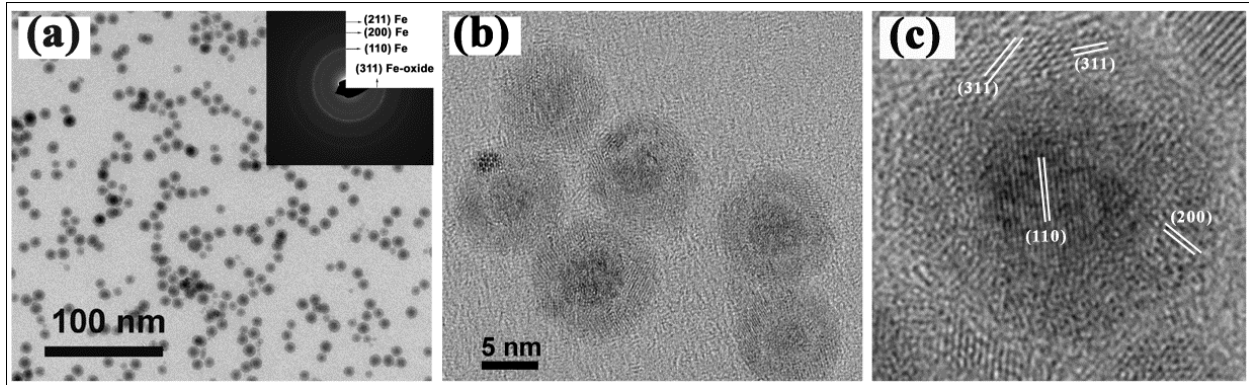


Figure 10: Bright field (a) TEM and (b,c) HRTEM images of Fe/ γ -Fe₂O₃ core-shell nanoparticles. Inset 1(a) shows selected area diffraction (SAD) pattern.

Figure 10 (a) shows a conventional bright field TEM image of these nanoparticles along with a (SAD) pattern in the inset. The average size of the nanoparticles is determined to be 9.8 ± 0.7 nm. Contrast variation at the interface clearly suggests a core and shell morphology in these nanoparticles. The (SAD) pattern is indexed to the structure of bcc iron and fcc iron-oxide. HRTEM images (Fig. 10 (b,c)) reveal the crystalline structure of both core and shell with lattice spacing of the core and shell corresponding to (110) planes of bcc iron and (311) planes of fcc iron oxide, respectively. The Fe core is single crystalline, however, the shell of γ -Fe₂O₃ is composed of small crystallites which are oriented randomly.

Figure 11 presents the temperature variation in magnetization (M) measured in 50 Oe under the zero-field cooled (ZFC), field cool-warming (FCW) and field cooled cooling (FCC) protocols. In the present case, there exists irreversibility in the ZFC and FCW curves even at room temperature, which suggests the presence of inter-particle interactions or some particles in the blocked state. It has been reported earlier that the FCW magnetization monotonically increases with decreasing temperature for SPMs, while it tends to saturate to a constant value or even decrease with decreasing temperature for super spin glass materials (SSGs). This feature in the FCW curve gives us a first indication that the nanoparticles show a collective glassy behavior at low temperature. There also exists a thermal hysteresis in the FCW and FCC curves below ~ 68 K. The onset of thermal hysteresis is marked by a sharp rise ($\sim T_g$) in $M_{FCC}-M_{FCW}$ as shown in inset (b).

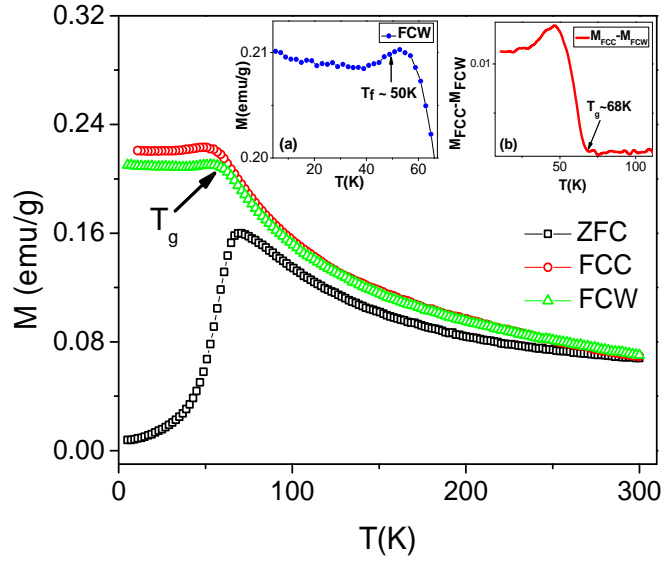


Figure 11: Temperature dependence of magnetization for zero-field-cooled (ZFC - \square -), field cooled-cooling (FCC - \circ -) and field cool-warming (FCW - Δ -). Insets: (a) the dip in M_{FCW} is associated with onset of spin freezing ($T_f \sim 50$ K) and (b) the difference ($M_{FCC}-M_{FCW}$) plotted against temperature, where a sharp rise ($T_g \sim 68$ K) marks the onset of thermal hysteresis.

To probe the spin dynamics of these nanoparticles, ac susceptibility measurements were systematically performed on the sample by applying an AC magnetic field of 10 Oe within the frequency (f) range of 10 Hz-10 kHz. By changing the frequency, we are deliberately changing the probe time ($\tau=1/f$) which allows us to probe the relaxation of particles in different time windows. In the inset of Figure 12a, the frequency dependence of real part of ac susceptibility (χ') is shown. The peak temperature (T_p) shifts to higher values as frequency increases, which is consistent with other reports [12]. An attempt to fit to Neel-Arrhenius (NA) law yielded unphysical results, as expected. This clearly indicates that the dynamics of these nanoparticles cannot be explained with a non-interacting particle model. Thus we extended our analysis to the Vogel-Fulcher (VF) model, which takes into account weak inter-particle interactions. According to the VF model, the relaxation time of an ensemble of weakly interacting nanoparticles follows eq. (1).

$$\tau = \tau_0 \exp \left[\frac{E_a}{k_B(T-T_0)} \right] \quad (1)$$

Here, E_a is the anisotropy energy barrier or the activation energy (KV) and τ_0 is the relaxation time of individual nanoparticle. The term T_0 is the characteristic temperature which gives a qualitative measure of the inter-particle interaction energy. The obtained fitted (Fig. 12a) parameters have reasonable values of $E_a/k_B = 571$ K, $\tau_0 = 6.9 \times 10^{-13}$ s and $T_0 = 48$ K. This successful fit confirms the presence of weak interactions in the nanoparticles that undergo collective freezing at $T_0 \sim 48$ K, henceforth referred to as freezing temperature (T_f). The fact that these nanoparticles fall in this range ($\sim 10^{-13}$ s) indicates that they individually relax like SPM particles above blocking temperature. However, in order to understand their collective behavior, the peak temperatures T_P are fitted to a critical power law (eq. 2)

$$\tau = \tau_0 \exp \left[\frac{T}{T_g} - 1 \right]^{-zv} \quad (2)$$

where T_g is the static spin glass temperature which marks the onset of critical slowing and collective glassy behavior; zv is the dynamical critical exponent which is related to the correlation length ξ that diverges at T_g . The use of such phenomenological activation law is usually done for cluster glass magnetic systems, especially SSG [13]. It is known from literature that for a SSG system [14, 15], the value of τ_0 ranges between 10^{-6} - 10^{-9} s. The obtained fit parameters for our nanoparticles are $\tau_0 = 2.8 \times 10^{-7}$ s, $T_g = 68$ K and $zv = 3.8$. The value of zv is very close to that calculated for 3D-Ising model³⁰ and the value of τ_0 further strengthens the case for SSG type of behavior.

Now the question that arises is, at what temperature does the crossover from SSG to SPM occur in the present system? The answer to this is rather non-trivial. Usually an ensemble of nanoparticles is said to be in the SPM state above the blocking temperature identified as the temperature corresponding to the peak in ZFC curve. This is true for mono-disperse nanoparticles with negligible or no interactions. But, in the case of nanoparticles with finite distribution in size, there is always a precursor effect associated with unblocking of smaller particles at temperatures lower than T_{P-ZFC} . Moreover, the presence of inter-particle interaction, formation of clusters further shifts T_{P-ZFC} to higher temperature. In case of core-shell nanoparticles, since the core and shell are composed of different materials, they have different magneto-crystalline anisotropy, thermal activation, uncompensated spins, lattice strain etc. Hence, all these factors together suggest that T_{P-ZFC} may not be the true blocking temperature, at least in case of core-shell nanoparticles. We define the mean blocking temperature ($\langle T_B \rangle$) as the temperature corresponding to the fastest change in the separation of ZFC from FCW curve, which, in turn is associated with the maximum number of nanoparticles unblocking as the temperature increases. This can be easily determined by identifying the peak position

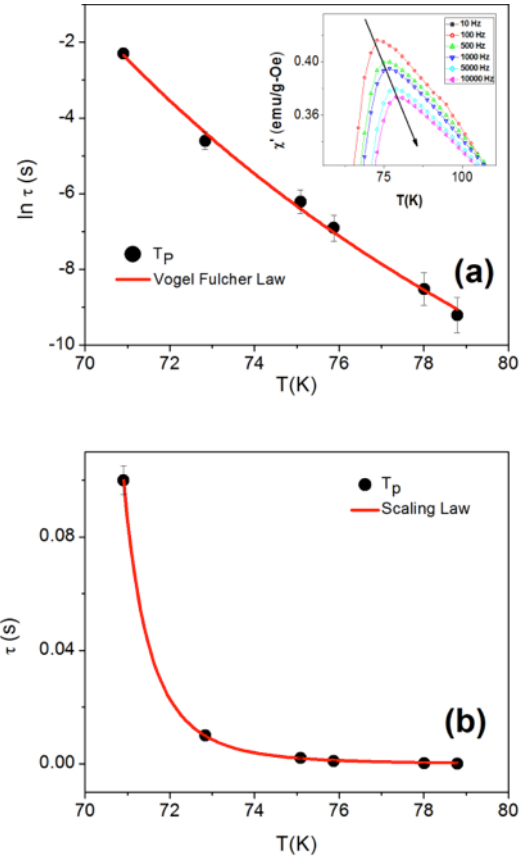


Figure 12: The best fit of the relaxation times (τ) to (a) the Vogel-Fulcher law and (b) the scaling law. Inset shows the frequency dependence of peak temperature (T_P) in χ' .

in $\frac{d(M_{FC}-M_{ZFC})}{dT}$. Figure 13a shows the $M(T)$ curves (left axis) measured at 100 Oe indicating the peak in ZFC curve (T_{P-ZFC}), while on the right axis, $-\frac{d(M_{FC}-M_{ZFC})}{dT}$ is plotted against temperature whose peak marks $\langle T_B \rangle$ as defined above. Figure 13b shows the magnetic field dependence of $\langle T_B \rangle$, separating the SSG from SPM region.

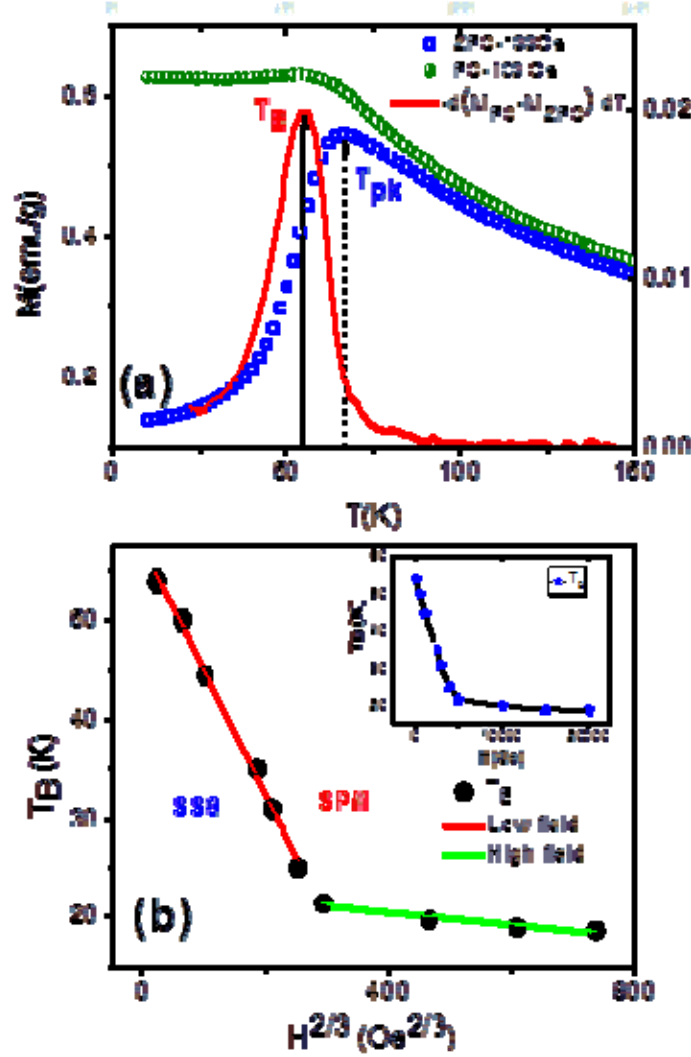


Fig 13. (a) ZFC/FC curve and the derivative $d[M_{FC}-M_{ZFC}]/dT$ indicating peak temperature of M_{ZFC} (T_{pk}) and mean blocking temperature (T_B); (b) Two straight AT-line fits for low and high field regime. Inset shows the evolution of blocking temperature (T_B) with measurement field.

Furthermore, we find that the freezing temperature $T_f \sim 48$ K as calculated from χ' corresponds to the freezing of the core (T_{f-cr}). Based on the same argument, the maximum at T_2 (~ 21 K) can be attributed to the freezing of shell (T_{f-sh}). This seems reliable since freezing temperature $T_{f-sh} \sim 21$ K is less than the mean blocking temperature of the shell ($T_{B2} \sim 24$ K)

calculated from the AT-line fit (Fig. 13b). Thus, we can identify two sets of mean blocking temperatures (T_{B1} , T_{B2}) and freezing temperatures (T_{f-cr} , T_{f-sh}) for the core and the shell respectively (Figure 14a,b).

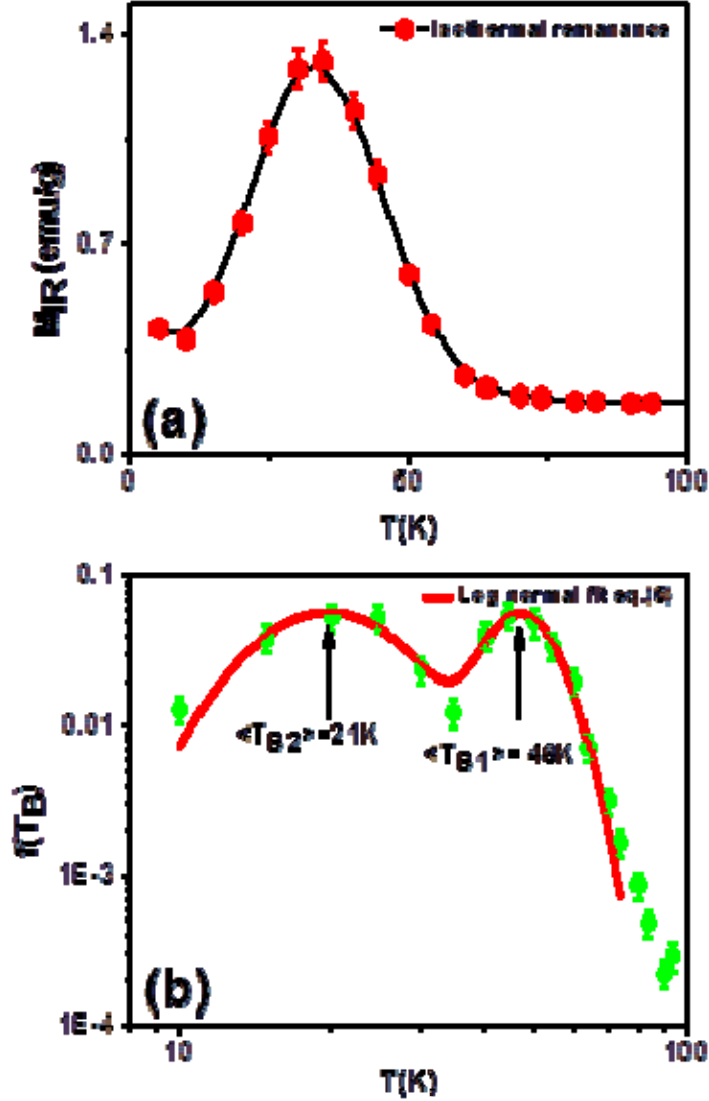


Fig 14. (a) Temperature dependence of isothermal remanance (b) Distribution function of T_B .

Our study, so far, gives us the first indication of possible SSG behavior below the identified glass transition temperature T_g . Currently, we are performing measurements to understand the SSG behavior in the core-shell nanoparticles to gain deeper insights into the magnetization dynamics. A rigorous study is being performed to distinguish the spin dynamics of the core and the shell separately which is both fundamentally and technologically important.

High-aspect ratio magnetic nanostructures for biosensor and microwave device applications

In past work, we have incorporated superparamagnetic (SPM) nanoparticles such as magnetite (Fe_3O_4) and cobalt ferrite (CoFe_2O_4) into a polymer matrix to create a new class of nanocomposite materials with tunable microwave response [16,17]. We propose that the microwave response can be further enhanced in high-aspect ratio magnetic nanostructures, such as carbon nanotubes (CNTs) filled with SPM nanoparticles [18], where the magnetic anisotropy can easily be tuned by varying the size and density of magnetic nanoparticles inside CNTs. Some of the main results for cobalt-ferrite and, more recently, nickel-ferrite based systems are reported here.

Synthesis of NiFe_2O_4 Nanoparticles

NiFe_2O_4 nanoparticles were synthesized using a thermal decomposition method [11] by mixing 1 mmol of nickel (II) acetylacetonate, 2 mmol of iron (III) acetylacetonate, 10 mmol 1,2-hexadecanediol, 6 mmol oleic acid, 6 mmol oleylamine, and 20 ml benzyl ether. The mixture was stirred magnetically in the presence of argon gas and was heated at 200°C for 2 hr and then refluxed at 300°C for 1 hr. The mixture was allowed to cool to room temperature by removing the heat source and 50 ml ethanol was added once cool. A black precipitate formed in the presence of ethanol and was centrifuged to collect the desired particles and remove any chemical waste. The black product was dissolved in hexane in the presence of oleic acid and oleylamine ($\sim 0.05\text{ml}$ each) to create a ferrofluid.

Results and discussion

The TEM image in Fig. 15 shows that the as-synthesized NiFe_2O_4 nanoparticles are 7 ± 2 nm in diameter. As evidenced by TEM images and magnetic data, nanoparticle agglomeration is not an issue with this sample. Magnetization vs. temperature curves ($M(T)$, FC and ZFC) reveal a T_B of ~ 34 K for the NiFe_2O_4 nanoparticles, shown in Fig. 16a. The $M(H)$ measurement at 300 K shows a curve with a saturation magnetization (M_s) of 31.5 emu/g and with zero coercivity (H_C), confirming SPM behavior of the NiFe_2O_4 nanoparticles at room temperature (Fig. 16b). It is clear from the zero-field cooled $M(H)$ data at 10K (Fig. 16c) that the NiFe_2O_4 nanoparticles have an H_C of 106 Oe. Fig. 16d shows FC $M(H)$ data at 10K ($H=1000$ Oe). From this data, we see an H_C of 84 Oe and no shift in the hysteresis loop.

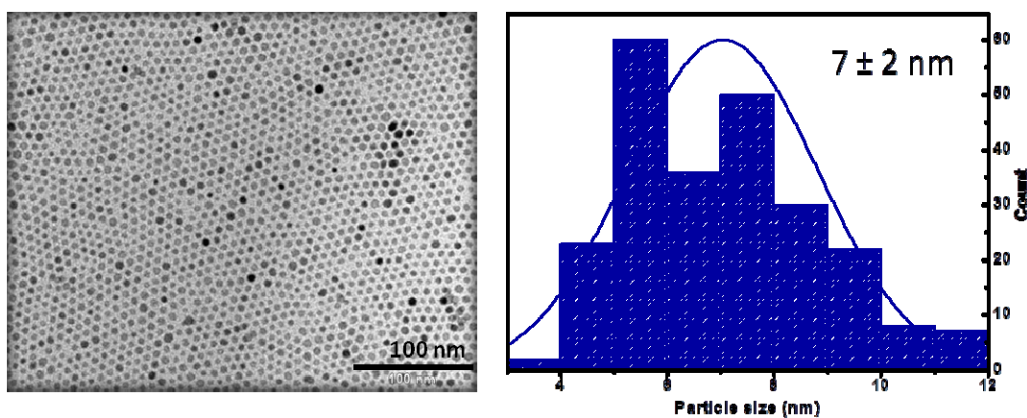


Figure 15: TEM image of nickel ferrite nanoparticles with histogram showing particle size of 7 ± 2 nm.

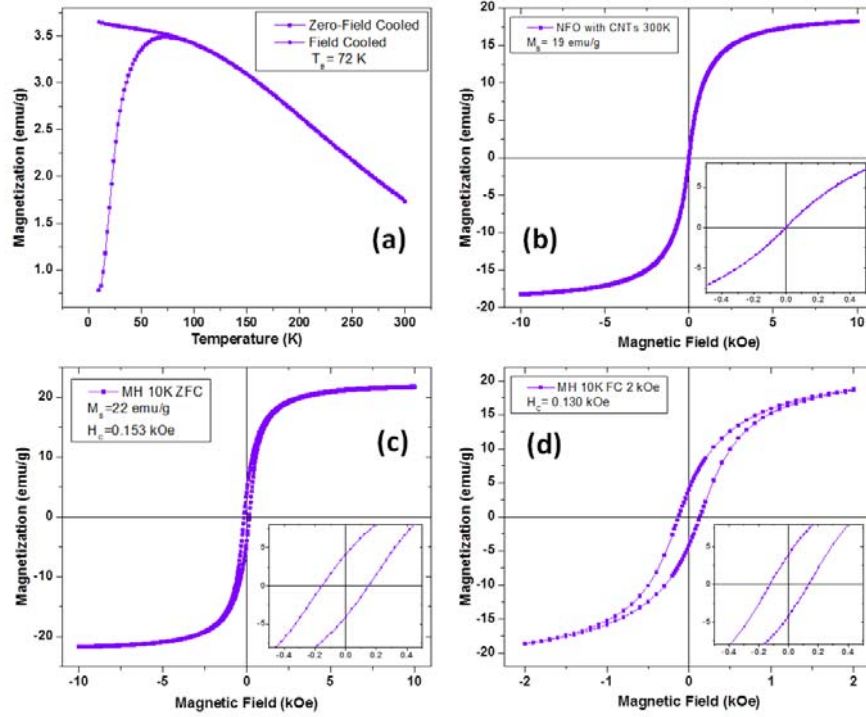


Figure 16: (a) $M(T)$ curves (field-cooled and zero-field cooled) from 10-300K showing a T_B of 34K; (b) $M(H)$ curve at 300 K with inset showing zero coercivity; (c) $M(H)$ curve at 10K (zero-field cooled) with inset showing a coercivity of 0.106 kOe; (d) $M(H)$ curve at 10K (field-cooled, 1kOe) shows a coercivity of 0.084 kOe and no hysteresis shift.

Temperature dependent ac susceptibility measurements (Fig. 17) were taken for free-standing NiFe₂O₄ nanoparticles. Results are currently being analyzed and fit to the proper models for this system. These NiFe₂O₄ nanoparticles were also placed in CNTs using the same method described above (for the CoFe₂O₄-filled CNTs). We expect for the NiFe₂O₄-based system to follow the same trends previously discovered by our lab in the Fe₃O₄ and CoFe₂O₄ systems with regard to the ac susceptibility measurements. Basic magnetic characterization is described below. $M(T)$ curves (FC and ZFC) reveal a T_B of ~72 K for the NiFe₂O₄-filled CNTs, shown in Fig. 18a. This is a large increase from the free-standing nanoparticles, which showed a T_B of ~34K. The $M(H)$ measurement at 300 K shows a curve with an M_s of 19 emu/g and $H_C = 0$, confirming SPM behavior of the NiFe₂O₄-filled CNTs at room temperature (Fig. 18b). It is clear from the zero-field cooled $M(H)$ data at 10K (Fig. 18c) that the NiFe₂O₄-filled CNTs have $H_C = 106$ Oe. Fig. 18d shows field-cooled $M(H)$ data at 10K ($H=2000$ Oe). From this data, we see that $H_C = 84$ Oe and there is no shift in the hysteresis loop.

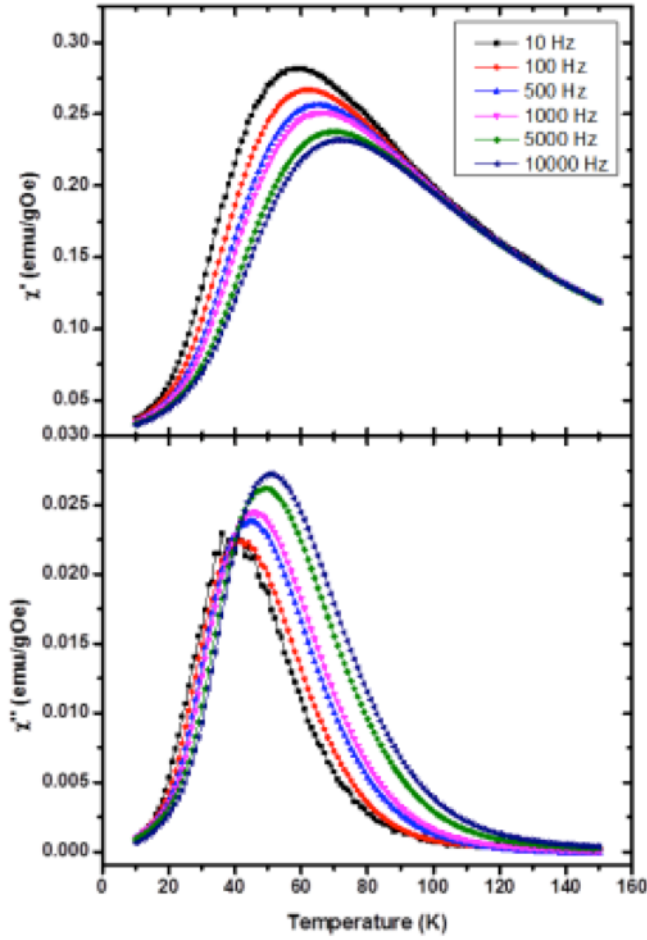


Figure 17: Temperature dependent AC susceptibility for NiFe_2O_4 nanoparticles.

We are planning to continue systematically investigating magnetic anisotropy and how it plays a key role in controlling the magnetic properties in nanoparticle assemblies. In addition to the standard DC and AC magnetization measurements with the PPMS, we will conduct resonant radio-frequency (RF) transverse susceptibility measurements and broadband microwave measurements using vector network analyzers on magnetic CNTs and magnetic CNTs-embedded in a polymer matrix.

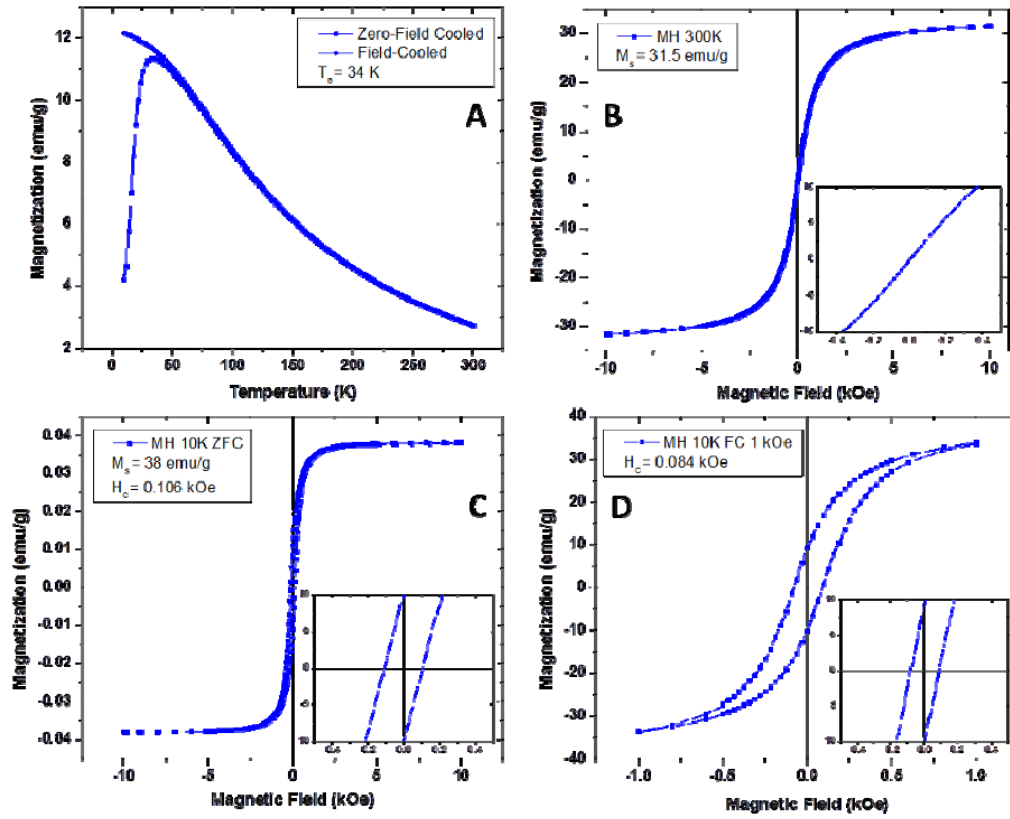


Figure 18: (a) $M(T)$ curves (FC and ZFC) from 10-300K showing a T_B of 72K; (b) $M(H)$ curve at 300 K with inset showing zero coercivity; (c) $M(H)$ curve at 10K (zero-field cooled) with inset showing a coercivity of 0.153 kOe; (d) $M(H)$ curve at 10K (field-cooled, 1kOe) shows a coercivity of 0.130 kOe and no hysteresis shift.

Tailoring the magneto-resistance, magneto-reactance and magneto-impedance effects in magnetic multi-wire systems for advanced magnetics sensor applications

The giant magneto-impedance (GMI) effect, which is defined as a large change in the AC impedance (Z) of a soft ferromagnetic conductor subject to an external dc magnetic field [18], forms the basis for developing stable, low cost, and environment friendly magnetic sensors for a variety of applications ranging from automobiles to biomedical engineering. It has been experimentally shown that soft ferromagnetic amorphous glass-coated microwires are one of the most attractive candidate materials for use in GMI-based sensors [18]. Interestingly, Garcia et al. [19] reported that both the GMI effect and its field sensitivity could be greatly improved in a system consisting of multiple wires in a parallel arrangement. Chiriac et al. [20] showed that this multi-wire system could have a great potential for highly sensitive detection of biomolecules. However, the origin of the observed GMI effect and the influence of wire spacing on the GMI signal remain to be investigated. From a magnetic sensor application perspective, it is essential to investigate the effects of multi-wire configuration on the magneto-impedance (MI), but also on the magneto-resistance (MR) and magneto-reactance (MX) of the system, both of which may provide alternative approaches for improving the field sensitivity of existing sensors.

To address these important issues, we have performed a systematic study of the MR, MX, and MI effects in an array of amorphous glass-coated $\text{Co}_{82.9}\text{B}_{3.4}\text{Si}_{5.8}\text{Mn}_{7.9}$ microwires. The amorphous wires were prepared by glass coated melt spinning technique [21]. The dc field from -120Oe to +120Oe and ac current of constant magnitude 5mA, over the frequency range 0.1 – 13 MHz were supplied along the sample axis. The impedance of all the samples was measured over the length of 10mm on the impedance analyzer HP4192A by four point technique. The MR, MX, and MI ratios were respectively calculated as

$$\frac{\Delta R}{R} = \frac{R(H) - R(H_{\max})}{R(H_{\max})} \times 100\% \quad (1)$$

$$\frac{\Delta X}{X} = \frac{X(H) - X(H_{\max})}{X(H_{\max})} \times 100\% \quad (2)$$

$$\frac{\Delta Z}{Z} = \frac{Z(H) - Z(H_{\max})}{Z(H_{\max})} \times 100\% \quad (3)$$

The dc magnetic field sensitivities of the MR, MX, and MI were respectively calculated as

$$\eta_R = 2 \times \frac{[\Delta R/R]_{\max}}{\Delta H} \times 100\% \quad (4)$$

$$\eta_X = 2 \times \frac{[\Delta X/X]_{\max}}{\Delta H} \times 100\% \quad (5)$$

$$\eta_Z = 2 \times \frac{[\Delta Z/Z]_{\max}}{\Delta H} \times 100\%, \quad (6)$$

where $[\Delta R/R]_{\max}$, $[\Delta X/X]_{\max}$, and $[\Delta Z/Z]_{\max}$ are the maximum values of the MR, MX, and MI ratios and ΔH is the full width at half maximum of the corresponding ratio versus H_{dc} plot.

Our studies reveal that the MR, MX, and MI ratios and their corresponding field sensitivities strongly depend on the number of microwires in an array and on the distance between them. As shown in Fig. 19, we have found that increasing the number of microwires increases the MR and MI ratios and their field sensitivities but decreases the MX ratio and field sensitivity. A similar trend is observed for the frequency dependence of these parameters. Increasing the distance between the wires is also found to decrease the MR, MX, and MI ratios of the array considerably. From a sensor application perspective, it is interesting to note that for the case of a single microwire [Fig. 19 (d-f)], the η_X reaches a value as high as 960 %/Oe at a frequency of 1 MHz, which is about 192 times the η_R and η_Z (~5 %/Oe), revealing the possibility of developing ultrahigh sensitivity magnetic field sensors based on the principle of the MX effect. These findings are of practical importance in developing single- and multi-wire systems for advanced sensor technologies. The important results have been published in *Journal of Alloys and Compounds* in 2012 (*In press*).

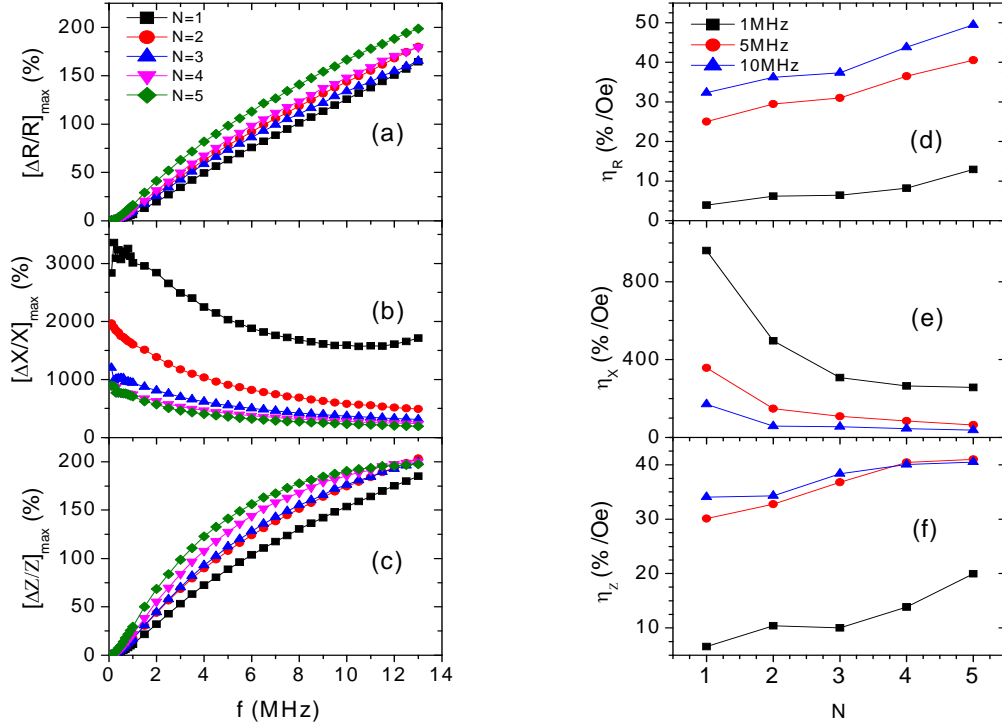


Figure 19: Frequency dependence of maximum MR (a), MX (b), and MI (c) ratios for N = 1, 2, 3, 4, and 5 and Corresponding field sensitivities (d-f) as a function of number of wires at frequencies f = 1, 5, and 10 MHz.

Detection of low concentration magnetic nanoparticles using a functional magnetic sensor based on radio frequency technology

Detection of cancer cells at their earliest stages in the human body, often before symptoms occur, can greatly increase the chances of successful treatment. For this purpose, several methods, such as visual identification of malignant changes, cell growth analysis, specific-ligand receptor labeling or genetic testing have been proposed [22]. However, these methods require lengthy and complicated analysis thus limiting them for practical use. A combination of magnetic sensors with magnetic nanoparticles offers an alternative approach for a highly sensitive, simple, and quick detection of cancer cells [23]. Improving the sensitivity of existing magnetic biosensors for detection of magnetic nanoparticles as biomarkers in biological systems is an important and challenging task.

Here we demonstrate the possibility of using the principles of radio frequency MR, MX, and MI effects to produce a functional magnetic biosensor with tunable and enhanced sensitivity. In our study, a biosensor prototype was designed by using an amorphous MATGLAS® 2714A ribbon and composition $\text{Co}_{65}\text{Fe}_4\text{Ni}_2\text{Si}_{15}\text{B}_{14}$ as a magnetic sensing element. It was covered by a thin parafilm paper. The ribbon piece was stacked on a non-magnetic glass support and placed at the center of a Helmholtz coil that provided a dc magnetic field ranging up to ± 120 Oe and parallel to its length. A driving current of magnitude 5 mA over the frequency range of 0.1 – 13 MHz was supplied along the ribbon axis, and the DC magnetic field induced magneto-impedance

(MI), magneto-resistance (MR), and magneto-reactance (MX) changes were measured by a four-probe technique on a HP4192A impedance analyzer over the length of 10 mm of the ribbon at room temperature. These measurements were performed for 20 μL of various concentrations (0, 124 pM, 1.24 nM, 12.4 nM, 62 nM, 124 nM, 620 nM, and 1.24 μM) of SPIO nanoparticles in water. The change in MR, MX, and MI with the applied field at a frequency of the driving current (also known as the MR, MX, and MI ratios) was calculated by using Equations (1-3). The changes in the MR, MX, and MI ratios due to the presence of SPIO nanoparticles at different concentrations were obtained by subtracting the corresponding responses observed for the blank prototype as,

$$\Delta \xi = [\xi]_{\max, \text{SPIO}} - [\xi]_{\max, \text{Blank}}, \quad (7)$$

where $[\xi]_{\max}$ with $\xi = \frac{\Delta R}{R}$, $\frac{\Delta X}{X}$, and $\frac{\Delta Z}{Z}$ are the maximum values of the MR, MX, and MI ratios in equations (1), (2), and (3) respectively.

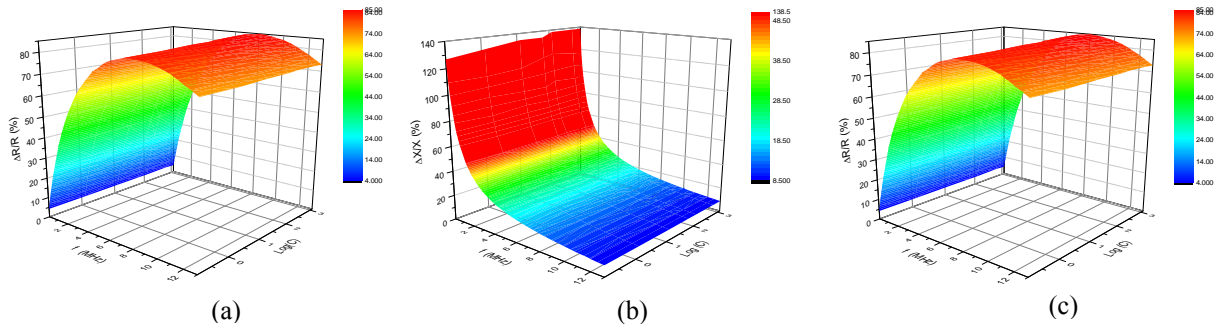


Figure 20: Frequency dependence of (a) MR, (b) MX, and (c) MI for various concentrations of Fe_3O_4 nanoparticles in water.

Through a systematic study of the magnetic particle (Fe_3O_4 , mean size ~ 7 nm) concentration dependence of MR, MX, and MI ratios of a soft ferromagnetic amorphous ribbon, we find that these ratios first increase sharply with increase in particle concentration (0 - 124 nM) and then become unchanged for higher concentrations (>124 nM) (Fig. 20 and Fig. 21).

These observations point to the existence of a certain sensing region and an upper limit to detection of the biosensor. While the biosensor with sensitivity optimized at a certain frequency can easily function using each principle, the MX-based biosensor shows the highest sensitivity. With this sensor, 3.6×10^{11} 7nm Fe_3O_4 nanoparticles can be detected over a detection area of $2.0 \times 10^7 \mu\text{m}^2$, which is comparable to a SQUID biosensor that

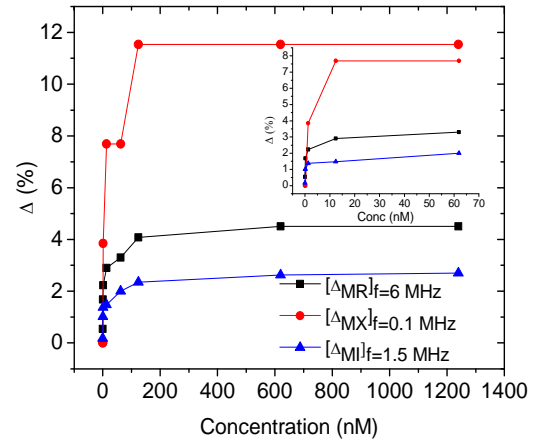


Figure 21: Sensitivity of MR, MX, and MI-based sensor for the detection of Fe_3O_4 nanoparticles with various concentrations in water.

detects the presence of 1×10^8 11nm Fe_3O_4 nanoparticles over a detection area of $6.8 \times 10^4 \mu\text{m}^2$. Given that the present biosensor works at room temperature, it is indeed promising for biosensing applications. *These interesting results are being collected and written for publication in Applied Physics Letters.* We are also in process of advancing experiments on Nanomag-D and Micromer-M surface-functionalized beads and live cell systems.

Giant magneto-impedance as a chemical sensing probe

At radio frequency region, it is known that the impedance Z of a soft ferromagnetic material is a function of the skin depth $\delta = \sqrt{\frac{\rho}{\pi \mu_T f}}$ (where ρ , μ_T , and f are the resistivity and the transverse permeability of the conductor and frequency of the driving current). This means that even at a fixed current frequency, the GMI of the conductor can be modified via the changes in resistivity and permeability [24-26]. This effect can arise due to the change in the magnetic anisotropy, material geometry, or any electrochemical changes. Since various aggressive chemicals can modify the surface of the magnetic electrode, to different extents, depending on their strength, the GMI of the conductor changes accordingly. This opens the possibility of using the GMI effect as a chemical sensing probe.

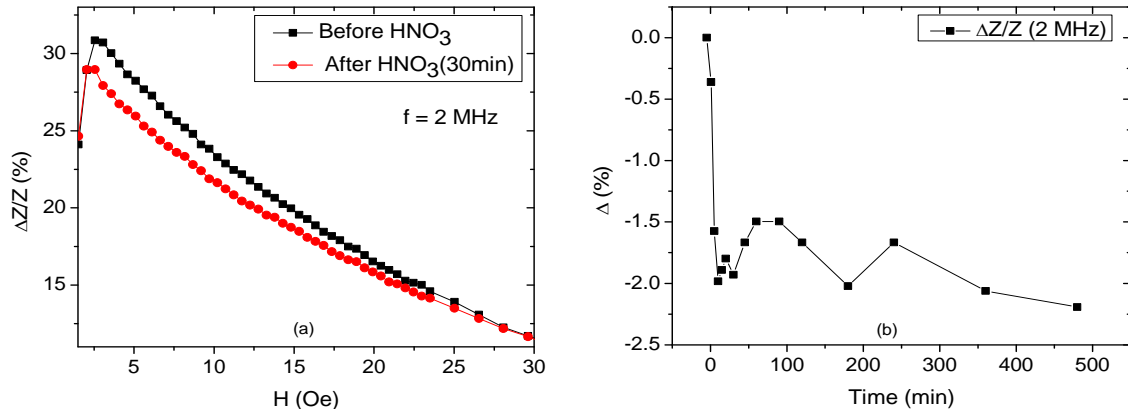


Figure 22: (a) GMI of amorphous ribbon before dropping HNO_3 and at 30 min after the dropping (b) Change in GMI with time with after the acid treatment relative to before treatment.

Here we demonstrate the magnetic label-free detection of the GMI-based sensor using a soft ferromagnetic amorphous ribbon. In this case, the magnetic permeability and hence the GMI of the ribbon changes due to the surface modification of the ribbon surface under corrosive fluids. Fig. 22 shows the change Δ in GMI of the amorphous ribbon at 2 MHz monitored with time when $5 \mu\text{L}$ of eight-fold diluted 70% HNO_3 is dropped on its surface of area $2.0 \times 10^7 \mu\text{m}^2$. We observed that the GMI ratio decreases with time, achieves a minimum value at certain time, and then remains almost constant beyond this time. The change in the GMI ratio and the time to achieve a stable value depends on the corrosive strength of the chemical. These results are promising in developing the GMI technology for chemical sensing applications. Our next step research is to conduct systematic studies for getting controllable changes in GMI of the ribbon due to surface modification by various chemicals of different concentrations.

Task II: Multifunctional composites for communication and energy applications

The aim of this task is to develop multilayer structures of ferroelectric and ferromagnetic thin films with high magnetoelectric coupling. Such structures can be used to develop biosensors where the sensitivity is determined by the degree of coupling between the magnetic and electric order parameters. The results presented in this report are directed towards optimization of the electrical polarization and the magnetic moment of the laser ablated films.

The successful optimization of the PZT thin film growth parameters allowed us to set the stage for doping PZT with rare earth elements such as La to further enhance its FE properties. It has been recently shown that in ABO_3 type materials a suitable ionic substitution, such as in Lanthanum (La)-doped PZT (PLZT) (where Pb^{2+} is substituted by La^{3+}), has a dramatic enhancement in the piezoelectric properties. There have been only a few recent reports on the growth of La-PZT films. However, most of the reports were based on chemical routes such as metal organic decomposition (MOD) and sol-gel method. This research represents one of the very few attempts to growth epitaxial La-PZT films using physical vapor deposition techniques.

Micro-structural properties of epitaxial PZT/CFO/LSMO thin films grown on MgO and STO substrates using the dual-laser ablation technique

In this report, we investigated the micro-structural properties of epitaxial PZT/LSMO bilayer thin films with the introduction of a thin $CoFe_2O_4$ (CFO) sandwich layer. The small lattice mismatch of CFO with LSMO, allowed for the epitaxial growth of the layers. Further, the recent demonstration of large magnetoelectric (ME) coupling in PZT/LSMO heterostructures based on a charge-mediated mechanism [27-29], in contrast to the strain-mediated coupling observed in ME composites, further made it a promising system for investigation [30-32]. With this in mind, a novel PZT/LSMO thin film structure with a CFO sandwich layer was deposited on single crystal $SrTiO_3$ (STO) (100) and MgO (100) substrates using the dual-laser ablation technique. Briefly, an excimer (KrF) laser (248 nm wavelength, 30 ns pulse full-width at half-maximum, (FWHM)) and a CO_2 laser (10.6 μm wavelength, 260 ns pulse FWHM) pulses were temporally and spatially overlapped on to the target surface during ablation. Stoichiometric ceramic targets of $La_{0.7}Sr_{0.3}MnO_3$, $CoFe_2O_4$, and $Pb(Zr_{0.52}Ti_{0.48})O_3$ (with 40 atomic % excess PbO to compensate for the Pb loss during ablation) were sequentially exposed to the laser beams inside the deposition chamber that was equipped with a custom-built multi-target carousel allowing the in-situ deposition of multilayers with clean interfaces. A distance of 4 cm was maintained between the substrate and the target during deposition. For the PZT/LSMO thin films, the initial LSMO bottom layer was deposited on STO and MgO substrates at 750 °C under a low ambient oxygen pressure (pO_2) of 10 mTorr, followed by the PZT top layer of 500 nm thickness deposited at 550 °C under a high pO_2 of 500 mTorr. For the PZT/CFO/LSMO thin films, after the deposition of the initial LSMO bottom layer under same conditions as in PZT/LSMO thin films, a thin layer of CFO of 50 nm thickness was deposited at 450 °C and pO_2 of 10 mT. This was followed by the PZT top layer under the same conditions as for PZT/LSMO thin films. For the ferroelectric measurements, LSMO top electrodes were deposited using a shadow mask that produced 100 μm contacts as shown schematically in Fig. 23 (a).

Fig. 23 (b and c) show the XRD θ - 2θ scans of PZT/CFO/LSMO heterostructures grown on STO and MgO (100) substrates, respectively. In both cases, only strong ($l00$) ($l = 1, 2$, and 3) diffraction peaks of PZT, CFO and LSMO were observed along with those of the single-crystal STO (100) and MgO (100) substrates confirming the epitaxial growth of the film in relation to the substrate. While the PZT peaks were indexed with the tetragonal phase with space group $P4mm$ (99), the CFO peaks matched with CFO face-centered-cubic (fcc) lattice with space group $Fd-3m$ (227).

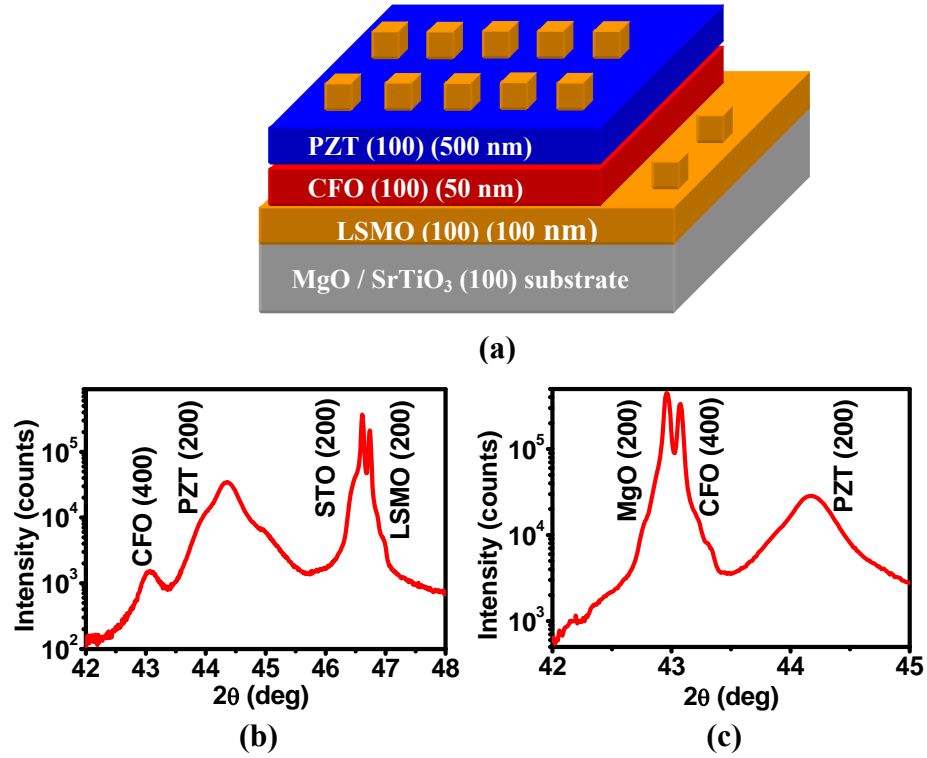


Figure 23: (a) Schematic diagram of PZT/CFO/LSMO heterostructure grown on MgO or STO (100) substrate and (b, c) XRD θ - 2θ scans of PZT/CFO/LSMO heterostructures grown on STO and MgO (100) substrates, respectively.

The interfacial microstructure in the PZT/CFO/LSMO thin film was analyzed using transmission electron microscopy (TEM) (FEI Tecnai F 20 S-Twin TEM). The sample for cross-sectional TEM analysis was prepared by milling a $5\ \mu\text{m} \times 10\ \mu\text{m}$ rectangular strip, 100 nm in thickness, from the film surface using a focused ion beam (FIB) (JOEL 4500 FIB/SEM) and Pt welding it to a TEM grid as shown in the series of SEM images in Fig. 24. First, a wedge pattern was milled into the film surface with high energy Ga ions using FIB and the resulting thin strip was Pt-welded onto the Omni probe (Fig. 24a) of the FIB. Second, the rectangular strip was carefully placed onto a Cu-made TEM grid (Fig. 24b). Finally, the Omni probe was detached from the TEM-ready sample (Fig. 24c) attached to the grid.

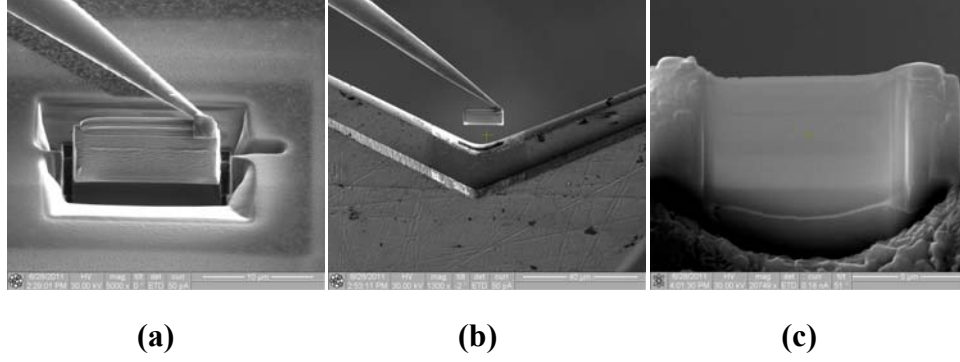


Figure 24: SEM images of (a) 5 μm x 10 μm rectangular strip milled from using a FIB from the surface of PZT/CFO/LSMO thin film, (b) attachment of the strip to the Cu TEM grid and (c) final milled sample attached to Cu grid ready for TEM analysis, respectively.

Fig. 25 shows a cross-sectional TEM image of the PZT/CFO/LSMO thin film on STO substrate and with LSMO top electrodes, respectively. From the image it is evident that the individual layers in the heterostructure are flat and of uniform thicknesses. This is associated with better thin film growth under dual-laser ablation as compared to traditional single-laser ablation. The individual layer thicknesses are 200 nm for the bottom LSMO layer, 50 nm for the CFO sandwich layer, 500 nm for the PZT top layer, and 100 nm for LSMO top electrode layer. The topmost layer is a protective coating of Pt that was used during the ion milling to preserve the structures underneath.

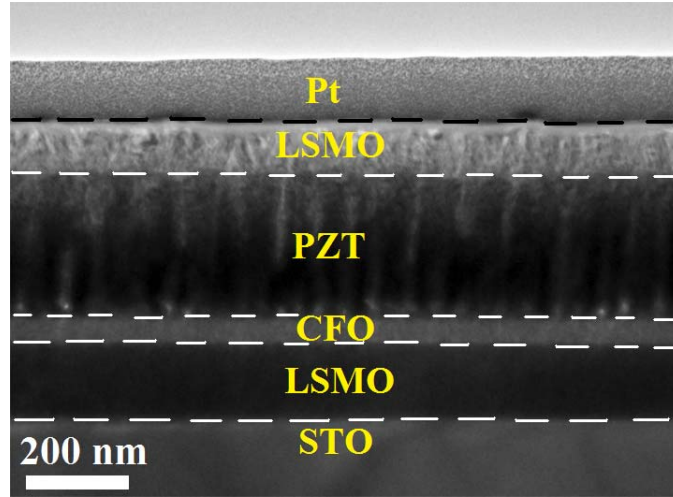


Figure 25: Cross-sectional TEM image of the PZT/CFO/LSMO heterostructure with the LSMO top electrode grown on STO (100) substrate using dual-laser ablation.

Fig. 26 (a, and c) shows high resolution TEM (HRTEM) cross-sectional images of the [110] crystallographic projections of the PZT-CFO and CFO-LSMO interfaces, respectively. The images clearly exhibit good epitaxial cube-on-cube growth morphology from LSMO to CFO (Fig. 26 c) and then from CFO to PZT (Fig. 26 a). The measured d-spacing values were consistent with those obtained from XRD. Both CFO-LSMO and PZT-CFO interfaces are atomically sharp. Fig. 26 (b) shows a typical selected area electron diffraction (SAED) pattern

taken from the epitaxial PZT/CFO/LSMO thin film on STO substrate near the PZT-CFO interface. The linear dotted SAED pattern corresponds to the single crystalline nature of the PZT and CFO layers. Due to the close lattice parameters of PZT and CFO a twining pattern (as shown by the red and yellow arrows) is observed in the SAED patterns. Such twining patterns were not observed in SAED patterns captured away from the interface excluding the possibility of defect-generated twin patterns. To illustrate the above, the SAED pattern for the LSMO layer in Fig. 26 (d) shows single crystal nature and cubic symmetry with no indication of twins. Similar single crystalline SAED patterns were observed for all layers corroborating the XRD observations.

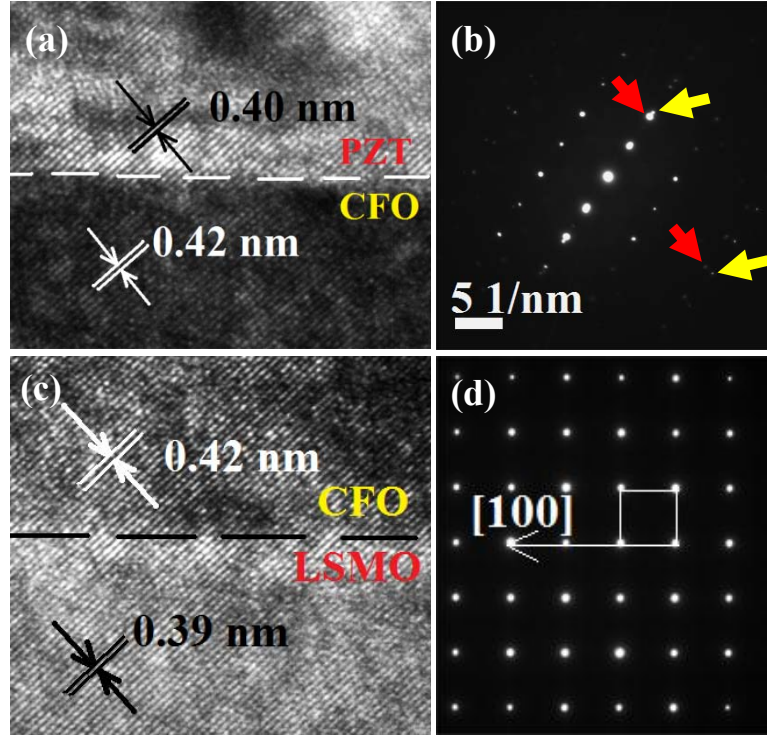


Figure 26: Cross-sectional HRTEM images and SAED patterns of (a, b) PZT-CFO interface and (c, d) CFO-LSMO interface for the PZT/CFO/LSMO heterostructure grown on STO (100) substrate.

Fig. 27 (a) shows the energy dispersive spectroscopy (EDS) under TEM for all elements in the PZT/CFO/LSMO heterostructure. Fig. 27 (b-e) shows the elemental line scans as a function of the cross-sectional film thickness measured from the bottom STO substrate (considered $< 0 \mu\text{m}$) to the top PZT layer (considered $> 0.5 \mu\text{m}$). From the analysis it is seen that while Sr signal is highest near the substrate, La and Mn signals are peak in the middle of the cross-section and Pb signal peaks at the top. This confirms the variation of chemical composition in the heterostructure as expected from the growth conditions.

In conclusion, PZT/CFO/LSMO heterostructures were grown on lattice matched single crystal MgO and STO (100) substrates. X-ray diffraction (XRD) revealed the single crystalline nature and the epitaxial relationship between the layers. Cross-sectional TEM analysis exposed atomically sharp and defect-free interfaces in the structure. Lattice parameters calculated from HRTEM images matched very well with those obtained from XRD analysis. Although the SAED patterns near the PZT-CFO interface exhibited single crystalline nature there was a presence of

twinning planes which were attributed to the slightly mismatched lattices of PZT and CFO, and not due to the presence of defects in the structure. EDS line scans performed along the cross-section of the film revealed the correct variation of elements as expected in the structure.

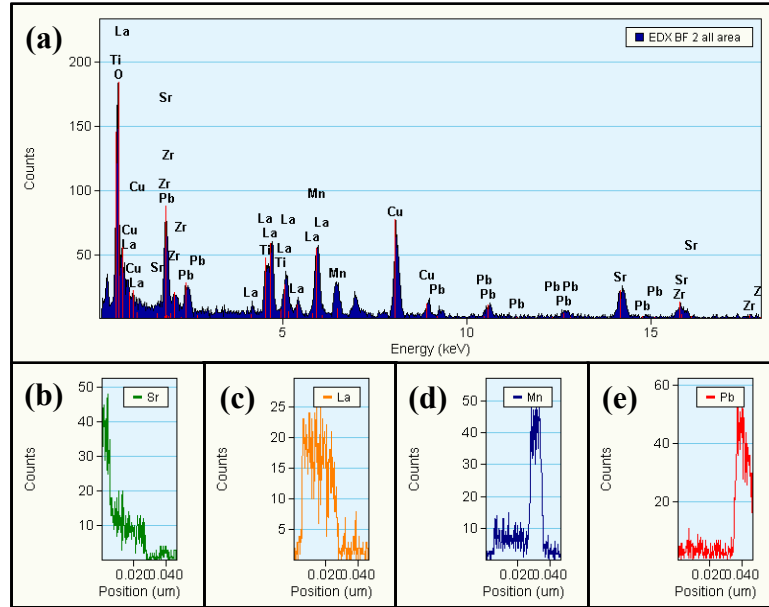


Figure 27: EDS under TEM for (a) all elements in the PZT/CFO/LSMO/STO heterostructure and (b-e) line-scans of individual elements as a function of cross-sectional film thickness starting from the bottom STO substrate to the top PZT layer for Sr, La, Mn and Pb, respectively.

After the successful growth and micro-structural analysis of the PZT/CFO/LSMO thin films as reported above, in future, further investigations into the ferromagnetic and ferroelectric properties of these heterostructures will be performed.

The successful optimization of the PZT thin film growth parameters allowed us to set the stage for doping PZT with rare earth elements such as La to further enhance its FE properties. It has been recently shown that in ABO_3 type materials a suitable ionic substitution, such as in Lanthanum (La)-doped PZT (PLZT), where Pb^{2+} is substituted by La^{3+} , has a dramatic enhancement in the piezoelectric properties [33]. There have been only few recent reports on the growth of La-PZT films. However, most of the reports were based on chemical routes such as metal organic decomposition (MOD) [34] and sol-gel method [35]. To our surprise, the growth of epitaxial La-PZT films using physical vapor deposition techniques has not been reported.

Growth and characterization of epitaxial La-modified PZT thin films on $SrTiO_3$ (100) and (111) substrates

We investigated the growth and characterization of epitaxial La-modified PZT thin films on $SrTiO_3$ (100) and (111) substrates using pulsed laser deposition (PLD) technique. La-PZT and undoped PZT films were deposited on 0.5 cm x 0.5 cm single crystalline $SrTiO_3$ (STO) (100) and STO (111) substrates for a thickness of 500 nm under similar conditions. In a typical

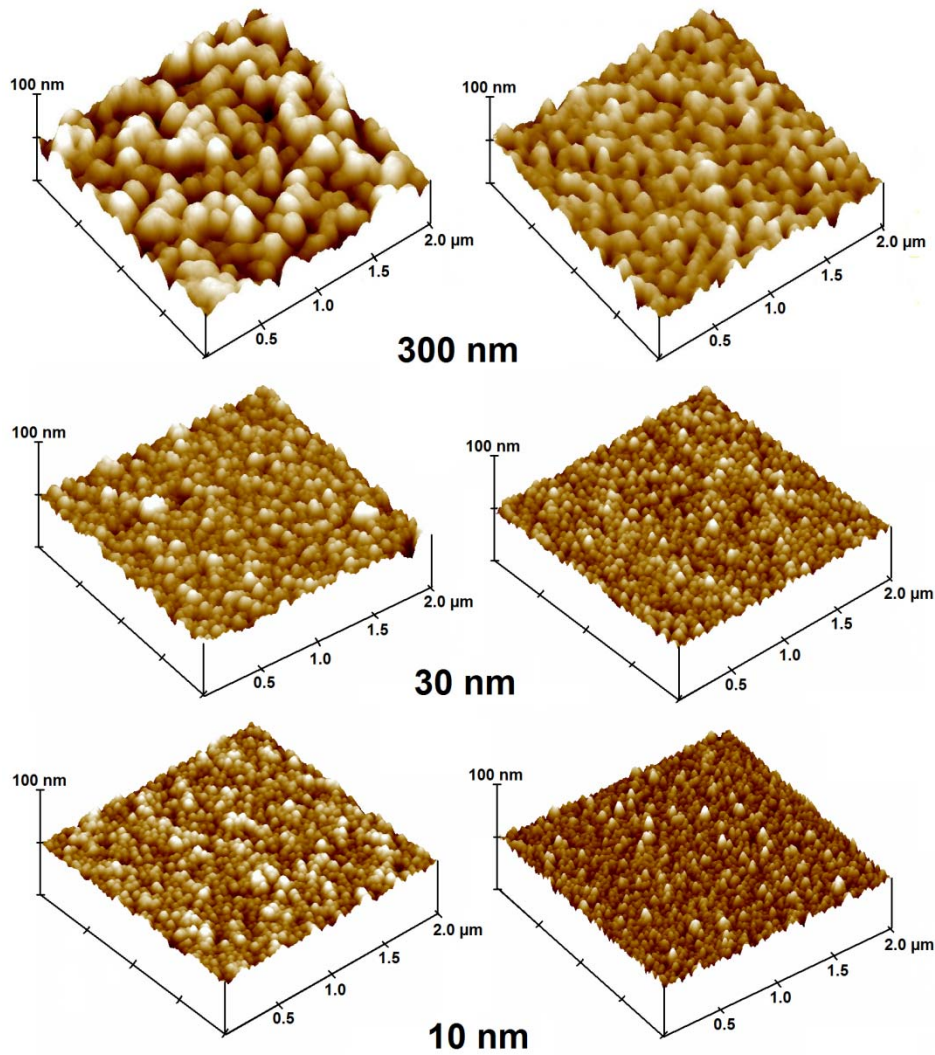


Figure 28. AFM images of PZT thin films deposited on SrTiO₃ (STO) (100) substrates, using single-laser (left column) and dual-laser (right column) ablations, for various film thicknesses of 300 nm, 30 nm, and 10 nm, respectively, showing the reduction in grain sizes and roughness for the dual-laser ablation process.

synthesis process, initially 100 nm thick epitaxial thin film of LSMO was deposited on the substrate to act as the bottom electrode which was followed by the PZT layer deposition. A shadow mask was used during PZT deposition to preserve an open access to the LSMO bottom electrode. After the PZT layer deposition, top LSMO electrodes of 100 μm in diameter were deposited in-situ using a shadow mask under the same conditions as the bottom LSMO electrodes. The structural properties for the as-deposited films were characterized using X-ray diffraction (XRD) for crystallinity and atomic force microscopy (AFM) for surface roughness. The polarization measurements were performed at room temperature (RT) using a Precision LC FE tester (Radiant Technologies, Inc). Leakage current densities (JL) in all the thin film capacitors were measured by applying a stress voltage of 9 V for a period of 1s (soak time).

Fatigue behavior was characterized by standard RT positive-up negative-down (PUND) testing by applying rectangular pulses at 10 kHz using ± 9 V peak voltages.

A series of PZT thin films were deposited on STO (100) substrates using both single and dual laser ablations to study the initial growth morphology and nucleation of grains. Figure 28 shows the AFM images exhibiting the surface morphologies of PZT films deposited for various film thicknesses of 300 nm, 30 nm, and 10 nm, respectively, showing the reduction in grain sizes and roughness for the dual-laser ablation process. While on one hand single-laser deposited PZT films (left column) showed increasing surface roughness (root-mean-square) values from $R_{\text{rms}} = 3.9$ nm for 10 nm film to $R_{\text{rms}} = 14.5$ nm for 300 nm film, on the other hand, dual-laser deposited PZT films (right column) showed almost similar surface roughness values from $R_{\text{rms}} = 4.1$ nm for 10 nm film to $R_{\text{rms}} = 5.5$ nm for 300 nm film.

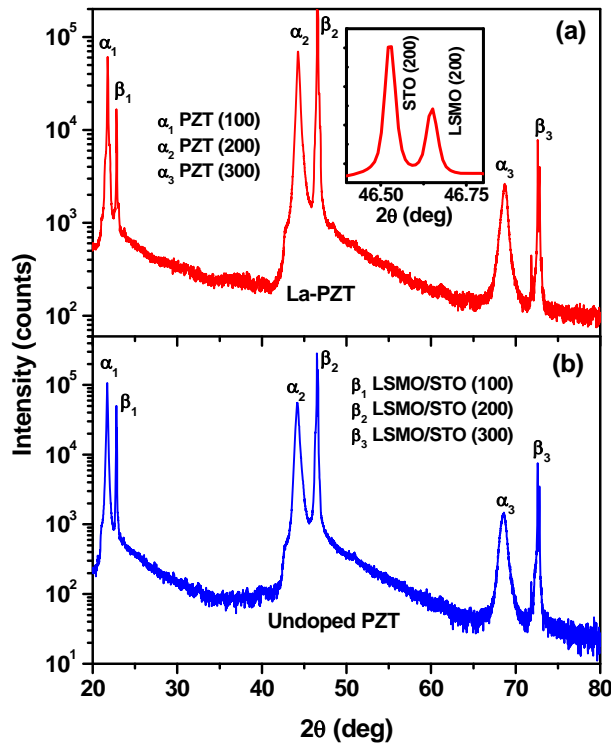


Figure 29. XRD patterns of (a) 0.1 at. % La doped PZT and (b) undoped PZT thin films deposited on SrTiO₃ (STO) (100) substrates using LSMO bottom electrodes, respectively. Inset to (a) shows the details of the LSMO (200) and STO (200) peaks.

XRD scans revealed the high quality and single crystalline nature of the as-deposited La-PZT films similar to undoped PZT thin films. Figure 29 shows XRD scans of La-PZT and undoped PZT films grown under the same conditions. In both cases, only strong (*l*00) (*l* = 1, 2, and 3) diffraction peaks of PZT were observed along with those of the single-crystal STO (100) substrates suggesting the epitaxial growth of the film in relation to the substrate. Secondary phase formations were not observed within the resolution limits of XRD. The data has been plotted in the log scale to intensify the presence of any secondary phases. The PZT peaks were indexed with the tetragonal phase with space group P4mm (99). No discernable peak shift was observed in the doped sample compared to the undoped.

Fig. 30 shows the polarization vs. applied voltage (P-V) hysteresis loops measured at different driving voltages from 5 V to 9 V for PZT thin films grown on (a) STO (100) and (b) STO (111) substrates. The coercive fields and remanent polarization (P_r) values changed as the drive voltage was increased. This suggested space charge effects in the measurements. On the other hand, similar voltage dependent polarization measurements performed on La-PZT films did not exhibited such effects. As seen in Fig. 31, the coercive field and P_r values remain almost unchanged once saturation was reached after 5 V drive voltage for the La-PZT films. This suggested that space charge effects were not significant in the polarization measurements.

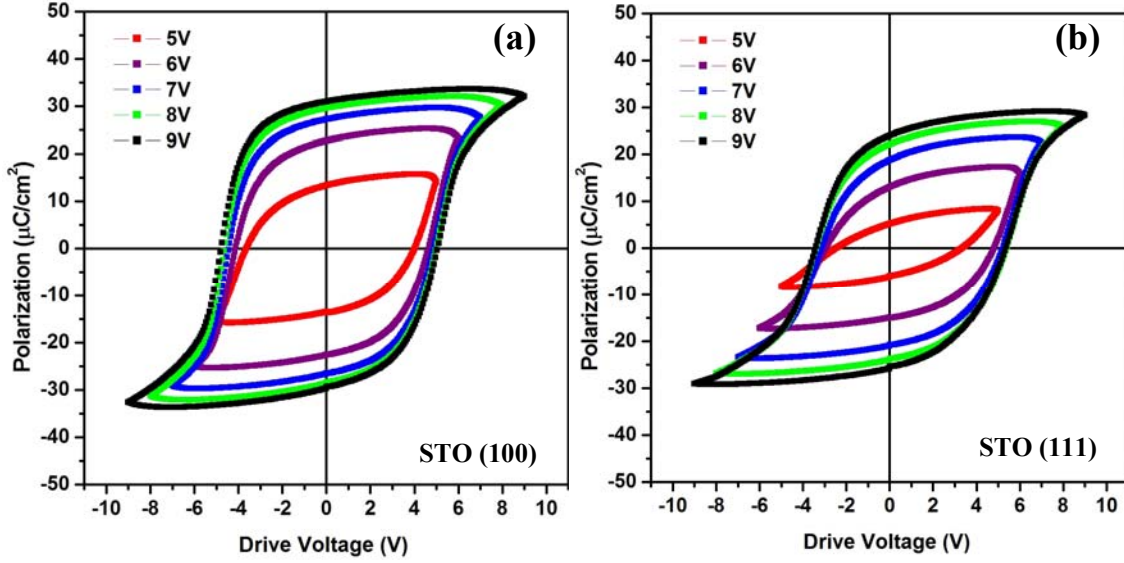


Figure 30: P-V hysteresis loops measured at different driving voltages from 5 V to 9 V for PZT thin films grown on (a) STO (100) and (b) STO (111) substrates.

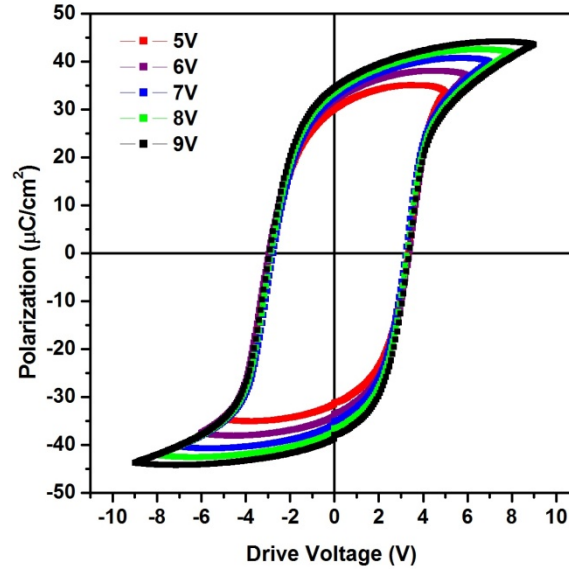


Figure 31: P-V hysteresis loops measured at different driving voltages from 5 V to 9 V for 0.1 at. % La doped PZT thin films.

Figure 32 shows the polarization versus electric field (P-E) hysteresis loops for 0.1 at. % La-doped PZT and undoped PZT thin films deposited under similar conditions on STO (100) substrates using LSMO top/bottom electrodes (as shown schematically). Data was measured at room temperature for a drive voltage of 9 V. Although there is a decrease in saturation polarization in the La-PZT curve as compared to the undoped PZT curve, there is a higher degree of squareness which could be related to the minimization of space charge effects due to La doping. Asymmetric P-E loops are associated with imprint failures in FE random access memories (RAM) due to built-in voltages. Higher degree of squareness as seen in La-PZT films is desirable for future memory applications.

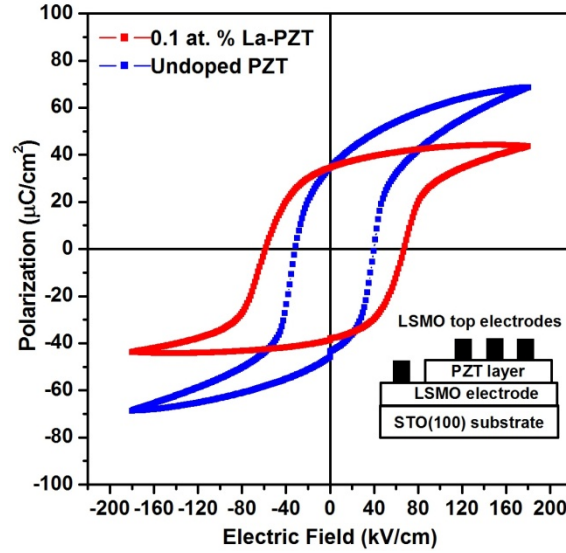


Figure 32: Polarization versus electric field (P-E) hysteresis loops for 0.1 at. % La doped PZT and undoped PZT thin films deposited under similar conditions on STO (100) substrates using LSMO top/bottom electrodes (as shown schematically). Data was measured at room temperature for a drive voltage of 9 V.

Conclusion

In conclusion, using a target of La-modified PZT with 30% excess PbO and a high fluence laser ablation process we have successfully grown La-PZT films with the desired perovskite structure and no impurity phases. Voltage dependent polarization measurements revealed an unchanging remanent polarization (P_r) which suggested that the space charge effects were not significant in the measurements. La-PZT films exhibited hysteresis loops with much higher degree of squareness (P_r/P_{max}) values as compared to undoped PZT films grown under the same conditions. In future we plan to study La-PZT thin films by changing the atomic percentage of La doping in the PZT target.

Task III – Solid-state materials for power conversion

High-performance nanofabricated thermoelectric materials for power generation:

While research on materials with improved properties continues, interest in correlated electron semiconductors for thermoelectric (TE) applications has recently accelerated following the discovery of the colossal Seebeck coefficient in FeSb₂ below room temperature.¹⁻³ The electrical and magnetic properties revealed in FeSb₂ may have technological implications for thermoelectric refrigeration [36-42] and spintronics [42-46]. Since the discovery of the colossal Seebeck coefficient [36,37] research on single crystal and bulk polycrystalline FeSb₂ has intensified [38-42, 44]. Most recently bulk FeSb₂ with spatially distributed Sb/InSb nanoinclusions have been synthesized by combining solid-state reaction of the elements with spark plasma sintering (SPS) [47]. However, when nano-scale grains are of interest, solid-state approaches do not always allow for simple control of the size of the grains or inclusions. Chemical syntheses allow for the processing of nanocrystals in a size-controlled and scalable manner, most useful in investigations of size-dependent TE properties [48-50]. Herein we report on a simple, low temperature solvothermal approach for the synthesis of FeSb₂ nanocrystals with space group *Pnnm* (No. 58), the structure type of interest for TE applications, and the resulting TE properties after consolidation of the nanocrystals employing SPS.

An investigation into nanostructured FeSb₂ has been mainly limited by the lack of a suitable preparative process. Nevertheless, there are a few reports on the synthesis of FeSb₂ nanocrystals by solution-based processes [51,52]. Recently the synthesis of FeSb₂ nanorods with the *Pnn2* crystal structure using surfactant molecules has been reported [52]. However, to the best of our knowledge, the synthesis of *Pnnm* FeSb₂ nanocrystals has yet to be reported. We have synthesized *Pnnm* FeSb₂ nanocrystals for the first time by using a surfactant and template free ethanol mediated solvothermal process. Analytical grades of iron (II) acetate (Fe(C₂H₃O₂)₂) and antimony (III) acetate (Sb(CH₃COO)₃) were used as the Fe and Sb sources, respectively. An excess molar quantity of Fe(C₂H₃O₂)₂ was always maintained in the solution because of the large difference in the reduction potential between Fe⁺² (Fe⁺² + 2e ↔ Fe, -0.409 V) and Sb⁺³ (Sb⁺³ + 3e ↔ Sb, 0.15 V). In a typical synthesis, 2 mmol of Fe(C₂H₃O₂)₂ and 2 mmol of Sb(CH₃COO)₃ were dissolved in 40 mL (80% volume of the custom made Teflon reactor) anhydrous ethanol. Three mmol sodium borohydride (NaBH₄) was added to the solution as a reducing agent. The entire solution was poured inside a custom made teflon reactor and tightly sealed. The teflon reactor was then inserted in a custom made stainless steel chamber and maintained at 220 °C for 16 h. At the end of the reaction, the chamber was gradually cooled to room temperature. The deep black precipitation (FeSb₂) at the bottom of the Teflon chamber was collected after washing first with 0.1 M HCl solution, then several times with distilled water and ACS grade alcohol. Finally the washed precipitate was dried in vacuum for 6 h and collected for characterization. This process yielded approximately half a gram of FeSb₂ nanocrystals. The synthesized FeSb₂ nanocrystals were characterized by X-ray diffraction (XRD, Bruker AXS D8 with Lynx Eye position sensitive detector), energy dispersive X-ray spectroscopy (EDS, Oxford Instruments INCA sight), and transmission electron microscopy (TEM, FEI Tecnai F20 S-Twin TEM). The specimen for TEM analysis was prepared by drop casting a very dilute dispersion of FeSb₂ nanocrystals in ethanol onto

carbon-coated 400 mesh copper grids. X-ray diffraction analyses confirmed the *Pnnm* FeSb₂ nanocrystals, and we intend to further characterize these materials as well as densify and measure the low temperature properties of dense nanocomposites.

Phase pure *Pnnm* FeSb₂ nanocrystals with an average size of 40 nm have been prepared by an ethanol mediated low temperature solvothermal process. No template or capping chemical was used in processing these nanocrystals, allowing the crystals to grow in their inherent orthorhombic symmetry. The *Pnnm* structure of the FeSb₂ nanocrystals was confirmed by XRD. The Figure 33 (a) shows the indexed XRD pattern of the as prepared FeSb₂ nanocrystals in comparison to the calculated XRD pattern for *Pnnm* FeSb₂. XRD of polycrystalline FeSb₂ after consolidation of the nanocrystals via SPS indicates that the *Pnnm* structure is retained after densification. No other XRD detectable impurity phases were present in the nanocrystals and in the densified specimen. EDS confirmed the formation of stoichiometric FeSb₂. The Figure 33 (b) also shows a low resolution TEM image of agglomerated FeSb₂ nanocrystals. The nanocrystals were nearly homogeneous in size, at 40 nm, polygonal in shape and resembled bipyramidal forms. Orthorhombic crystal forms were preferred for the FeSb₂ nanocrystals presumably because no surfactant or template molecules were used in the reaction process to control the shape of the nanocrystals. Selected Area Electron Diffraction (SAED) patterns showed linear dot patterns (c), indicating that the FeSb₂ nanocrystal are single crystals. The SAED pattern also confirmed the d-spacings of the major diffraction planes of *Pnnm* FeSb₂ (not shown in the figure). The presence of twin diffraction spots in the SAED pattern (shown by arrows in c) are from lattice planes with the same diffraction angle, also indicated in Figure 33a. Lattice fringe spacings (d) correspond to (111) planes.

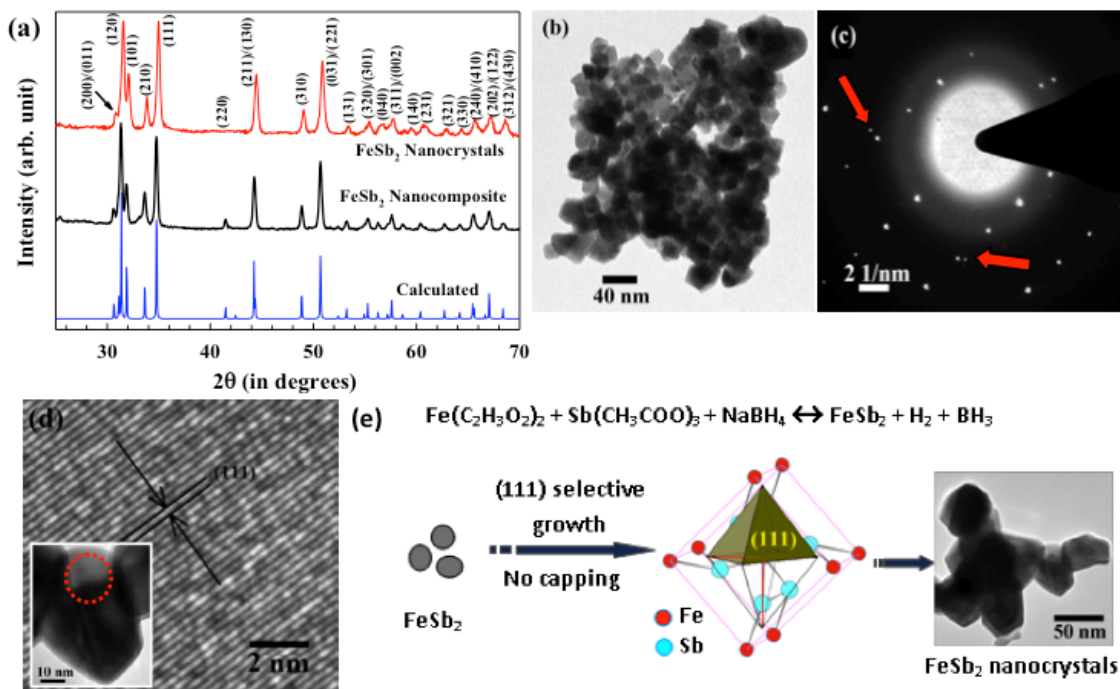


Figure 33: (a) XRD pattern of the as prepared FeSb₂ nanocrystals, (b) TEM image of agglomerated FeSb₂ nanocrystals, (c) Selected Area Electron Diffraction (SAED) patterns, and (d) lattice fringe spacings (d) correspond to (111) planes.

III. Reportable Outcomes

Publications and presentations in the 2011-2012 duration acknowledging support from CIFM through grant USAMRMC W81XWH-07-1-0708 and Continuation grant USAMRMC W81XWH1020101/3349 (Participating CIFM faculty and postdoctoral contributors are shown in bold, while CIFM student contributors are italicized):

Journal Publications:

1. **H. Khurshid**, W. Li, **M.H. Phan**, **P. Mukherjee**, **H. Srikanth**, and G.C. Hadjipanayis, “Surface spin disorder and exchange-bias in hollow maghemite nanoparticles”, *Applied Physics Letters* **101**, 022403 (2012)
2. *S. Chandra*, **H. Khurshid**, W. Li, G. C. Hadjipnays, **M. H. Phan**, and **H. Srikanth**, “Spin dynamics and criteria for onset of exchange bias in superspin glass Fe/ γ -Fe₂O₃ core-shell nanoparticles”, *Physical Review B* **86**, 014426 (2012)
3. *A. Chaturvedi*, *K. Stojak*, *N. Laurita*, **P. Mukherjee**, **H. Srikanth** and **M. H. Phan**, “Enhanced magnetoimpedance effect in Co-based amorphous ribbons coated with carbon nanotubes”, *Journal of Applied Physics* **111**, 07E507 (2012)
4. *S. Chandra*, *A. I. Figueroa*, *Barnali Ghosh*, *A. K. Raychaudhuri*, **M. H. Phan**, **P. Mukherjee** and **H. Srikanth**, “Fabrication and magnetic response probed by RF transverse susceptibility in La_{0.67}Ca_{0.33} MnO₃ nanowires”, *Physica B: Condensed Matter* **407**, 175 (2012)
5. **D. Mukherjee**, *R. Hyde*, **P. Mukherjee**, **H. Srikanth**, and **S. Witanachchi**, “Role of dual-laser ablation in controlling the Pb depletion in epitaxial growth of Pb(Zr_{0.52}Ti_{0.48})O₃ thin films with enhanced surface quality and ferroelectric properties”, *Journal of Applied Physics* **111**, 064102 (2012).
6. **D. Mukherjee**, *N. Bingham*, **M. H. Phan**, **H. Srikanth**, **P. Mukherjee**, and **S. Witanachchi**, “Ziz-zag interface and strain-influenced ferromagnetism in epitaxial Mn₃O₄/La_{0.7}Sr_{0.3}MnO₃ thin films grown on SrTiO₃ (100) substrates”, *J. Appl. Phys.* **111**, 07D730 (2012).
7. **D. Mukherjee**, **P. Mukherjee**, **H. Srikanth**, and **S. Witanachchi**, “Carrier-mediated Interaction of Magnetic Moments in Oxygen Vacancy Controlled Epitaxial Mn doped ZnO Thin Films.”, *J. Appl. Phys.* **111**, 07C318 (2012).
8. **A. Datta**, *A. Popescu*, **L. Woods**, and **G.S. Nolas**, ‘The Bottom-Up Approach To Bulk Thermoelectric Materials with Nano-Scale Domains’, Ch. 14, *CRC Handbook: Thermoelectrics and its Energy Harvesting*, edited by D.M. Rowe, CRC Press, Boca Raton, 2012.

9. **A. Datta** and **G.S. Nolas**, ‘Solution-Based Synthesis & Low-Temperature Transport properties of CsBi_4Te_6 ’, *Applied Materials & Interfaces*. **4**, 772 (2012).
10. **A. Datta** and **G.S. Nolas**, ‘Synthesis and Characterization of Nanocrystalline FeSb_2 for Thermoelectric Applications’, *Eur. J. Inorg. Chem.* **55** (2012).
11. N.H. Hong, C.-K. Park, A. T. Raghavender, O. Ciftja, *N.S. Bingham*, **M.H. Phan**, and **H. Srikanth**, “Room temperature ferromagnetism in monoclinic Mn-doped ZrO_2 thin films”, *Journal of Applied Physics* **111**, 07C302 (2012).
12. *N.S. Bingham*, *P. Lampen*, T.L. Phan, **M.H. Phan**, S.C. Yu, and **H. Srikanth**, “Magnetocaloric effect and refrigerant capacity in $\text{Sm}_{1-x}\text{Sr}_x\text{MnO}_3$ ($x=0.42, 0.44, 0.46$) manganites”, *Journal of Applied Physics* **111**, 07D705 (2012).
13. *P. Lampen*, A. Puri, **M.H. Phan**, and **H. Srikanth**, “Structure, magnetic, and magnetocaloric properties of amorphous and crystalline $\text{La}_{0.4}\text{Ca}_{0.6}\text{MnO}_{3+\delta}$ nanoparticles”, *Journal of Alloys and Compounds* **2012**; 94:512.
14. *A. Popescu*, **A. Datta**, **G. S. Nolas**, and **L. M. Woods**, ‘Thermoelectric properties of Bi-doped PbTe composites’, *Journal of Applied Physics* **109**, 103709 (2011).
15. *A. Chaturvedi*, *S. Stefanoski*, **M.H. Phan**, **George S. Nolas**, and **H. Srikanth**, “Table-like magnetocaloric effect and enhanced refrigerant capacity in $\text{Eu}_8\text{Ga}_{16}\text{Ge}_{30}$ -EuO composite materials”, *Applied Physics Letters* **2011**; 99:162513.
16. **M.H. Phan**, V. Franco, *A. Chaturvedi*, *S. Stefanoski*, **G.S. Nolas**, and **H. Srikanth**, “Origin of the magnetic anomaly and tunneling effect of europium on the ferromagnetic ordering in $\text{Eu}_8\text{Ga}_{16}\text{Ge}_{30}$ type-I clathrates”, *Physics Review B* **2011**; 84:054436.
17. *J. Devkota*, *A. Ruiz*, **P. Mukherjee**, **H. Srikanth**, and **M.H. Phan**, “Magneto-resistance, magneto-reactance, magneto-impedance effects in single and multi-wire systems”, *Journal of Alloys and Physics* **2012** (in press)
18. *A. Ruiz*, *A. Chaturvedi*, A.T. Le, **P. Mukherjee**, **H. Srikanth**, and **M.H. Phan**, “Magneto-impedance effect in electrodeposited Cu/FeNi/Cu/FeNi multilayer wires”, *Physica B: Condensed Matter* **2012** (accepted)
19. *S. Chandra*, **H. Khurshid**, **M.H. Phan**, and **H. Srikanth**, “Asymmetric hysteresis and its dependence on magnetic anisotropy in exchange biased Co/CoO core-shell nanoparticles”, *Applied Physics Letters* **2012** (under review)
20. *J. Devkota*, *A. Ruiz*, **P. Mukherjee**, C. Wang and S. Mohapatra, **H. Srikanth**, and **M.H. Phan**, “Detection of low concentration magnetic nanoparticles using a functional biosensor based on radio frequency technology”, *Applied Physics Letters* **2012** (in preparation)

21. *A. Ruiz, A. Chaturvedi, K. Stojak* , **P. Mukherjee, H. Srikanth** and **M. H. Phan**, “Magneto-impedance as Chemical and Biosensing Probes”, *Sensors* – 2012 (Invited paper, in preparation).

Conference Presentations:

1. *J. Devkota, A. Ruiz, H. Khurshid, A. Chaturvedi, A. Puri, P. Mukherjee, H. Srikanth, M.H. Phan*, “Detection of Functional Magnetic Nanoparticles using Ferromagnetic Microwires-based Giant Magneto-impedance Sensors”, Nano-Bio Collaborative International Conference, March 22-24, 2012, Tampa, Florida, USA
2. *A. Ruiz, J. Devkota, A. Chaturvedi, K. Stojak, P. Mukherjee, H. Srikanth, M.H. Phan*, “GMI sensors with superparamagnetic nanoparticles for highly sensitive detection of cancer cells and biomolecules”, Nano-Bio Collaborative International Conference, March 22-24, 2012, Tampa, Florida, USA
3. *K. Stojak, P. Mukherjee, H. Srikanth, M.H. Phan*, “Synthesis of carbon nanotubes filled with magnetic nanoparticles for biomedical applications”, Nano-Bio Collaborative International Conference, March 22-24, 2012, Tampa, Florida, USA
4. *K. Stojak, S. Chandra, A. Ruiz, M.H. Phan, P. Mukherjee, and H. Srikanth*, “Filled Carbon Nanotubes with Novel Magnetic Properties for Biomedical Applications”, NanoFlorida Conference, September 28-29, 2012 Tampa, Florida, USA.
5. *J. Devkota, A. Ruiz, P. Mukherjee, H. Srikanth, M.H. Phan, C. Wang and S. Mohapatra*, “Amorphous Ribbon-based Magnetic Biosensor with Enhanced Sensitivity for Highly Sensitive Detection of Nanomag-D Beads”, NanoFlorida Conference, September 28-29, 2012 Tampa, Florida, USA.
6. *A. Ruiz, J. Devkota, P. Mukherjee, H. Srikanth, M.H. Phan*, “Improving the magnetic response of giant magneto-impedance in single and multi-wire systems”, NanoFlorida Conference, September 28-29, 2012 Tampa, Florida, USA.
7. **G.S. Nolas**, ‘A Bottom-up Approach for Nanostructured Thermoelectrics, Invited, 9th European Conference on Thermoelectrics, September 30, Thessaloniki, Greece, 2011.
8. *A. Popescu, A. Datta, G.S. Nolas and L. Woods*, ‘Tailoring Thermoelectric Properties of Bismuth: Theoretical Investigations’, American Institute of Physics Conference Proceedings 1449, 9th European Conference on Thermoelectrics, pp. 45 – 48, 2012.
9. **G.S. Nolas**, ‘Synthesis and Characterization of Nanostructured Thermoelectric Materials Prepared by a Two-step Bottom-up Synthetic Process’, European Materials Research Society Conference, May 15, Strasbourg, France, 2012.
10. **D. Mukherjee, M. Hordagoda, R. Hyde, P. Mukherjee, H. Srikanth, S. Witanachchi**, Dual Laser Ablation: A Novel Technique for the In-situ Growth of Epitaxial Multiferroic Heterostructures of Ultra-thin Films”, *NANOSMAT-USA*, Tampa, FL, (March 27th to 30th, 2012)

11. *C.L. Hettiarachchi, D. Ferizovic, D. Mukherjee, R. Hyde, S. Witanachchi, P. Mukherjee*, “Structural and Optical Properties of Surfactant-free Coatings of PbSe Quantum Dots deposited by a Laser Assisted Spray Process” *NANOSMAT-USA*, Tampa, FL, (March 27th to 30th, 2012)
12. *M. Hordagoda, D. Mukherjee, R. Hyde, P. Mukherjee, S. Witanachchi*, “Growth and Characterization of Epitaxial Pb(Zr_{0.52}Ti_{0.48})O₃ Ultra-thin Films using a Novel Dual-Laser Deposition Technique”, *NANOSMAT-USA*, Tampa, FL, (March 27th to 30th, 2012)
13. *A. Datta, K. Wei, A. Popescu, L. Woods and G.S. Nolas*, ‘Processing Dependence on the Thermoelectric Properties of Nanostructured Thermoelectric Materials’, Materials Research Society Conference, November 29, Boston, Massachusetts, 2011.
14. *A. Chaturvedi, N. Laurita, K. Stojak, M.H. Phan, P. Mukherjee, and H. Srikanth*, “Carbon nanotube-based gas sensors using the magnetoimpedance effect”, 56th Annual MMM Conference on Magnetism and Magnetic Materials, October 30 to November 3, 2011, Scottsdale, Arizona, USA.
15. *N. Laurita, A. Chaturvedi, P. Jayathilaka, M.H. Phan, H. Srikanth, and C. W. Miller*, “Impact of field-induced exchange anisotropy on the magnetoimpedance effect in FeMn/Metglas ribbons bilayer structures”, 56th Annual MMM Conference on Magnetism and Magnetic Materials, October 30 to November 3, 2011, Scottsdale, Arizona, USA.
16. *D. Mukherjee, N. Bingham, M.H. Phan, H. Srikanth, P. Mukherjee and S. Witanachchi*, “Ziz-zag interface and strain-influenced ferromagnetism in epitaxial Mn₃O₄/La_{0.7}Sr_{0.3}MnO₃ thin films grown on MgO (100) and SrTiO₃ (100) substrates”, 56th Annual MMM Conference on Magnetism and Magnetic Materials, October 30 to November 3, 2011, Scottsdale, Arizona, USA.
17. *A. Chaturvedi, S. Stefanoski, M. H. Phan, G.S. Nolas, and H. Srikanth*, “Table-like magnetocaloric effect and enhanced refrigerant capacity in clathrate-based composite materials”, 56th Annual MMM Conference on Magnetism and Magnetic Materials, October 30 to November 3, 2011, Scottsdale, Arizona, USA.
18. *N.S. Bingham, M.H. Phan, H. Srikanth, C.L. Zhang, and S.W. Cheong*, “Multiphase transitions and complex phase diagram in mixed phase (La,Pr,Ca)MnO₃ manganites”, 56th Annual MMM Conference on Magnetism and Magnetic Materials, October 30 to November 3, 2011, Scottsdale, Arizona, USA.
19. *K. Stojak, S. Pal, H. Srikanth, C.Morales, J. Dewdney, J.Wang and T.Weller*, “Magnetic Polymer Nanocomposites with Tunable Microwave and RF Properties”, 56th Annual MMM Conference on Magnetism and Magnetic Materials, October 30 to November 3, 2011, Scottsdale, Arizona, USA.
20. *N.S. Bingham, T.L. Phan, M.H. Phan, S.C. Yu and H. Srikanth*, “Phase coexistence and magnetocaloric effect in Sm_{1-x}Sr_xMnO₃ (x = 0.42, 0.44, 0.46) manganites”, 56th Annual

MMM Conference on Magnetism and Magnetic Materials, October 30 to November 3, 2011, Scottsdale, Arizona, USA.

21. **G.S. Nolas**, 'New Crystal Growth Techniques in Investigating Single-crystal Inorganic Clathrates', Invited, to be presented at the Collaborative Conference on Crystal Growth, Orlando, Florida, December 11-14, 2012.

IV. Conclusion

Update on Milestones and their Status:

1. Chemical synthesis of magnetic nanoparticles and ferrofluids, Structural analysis, DC and AC magnetization studies.
Completed in year 1
2. Functionalization of ferrofluids with biocompatible surfactant coatings of the nanoparticles. Chemical and Physical properties characterization of the functionalized ferrofluids.
Completed in year 2
3. Studies of magnetic and hydrodynamic properties of bio-functionalized ferrofluids under flow conditions.
Completed in year 3
4. Synthesis of PEG, Dextran coated nanoparticles and clusters for hyperthermia experiments and their structural and magnetic characterization.
Initiated in year 4, ongoing.
5. Measurements and comparative analysis of specific absorption rates and AC power losses of ferrofluids for magnetic hyperthermia applications.
Initiated in year 4, ongoing.
6. Bifunctional metal-oxide coupled and core-shell nanostructures
Initiated in year 4, completed in year 5.
7. Synthesis and characterization of Au templates with variable spacing and formation of In nano-pore structures.
Completed in year 1
8. Growth of nano-wires of inorganic compounds with variable diameters.
Completed in year 3
9. Formation of polymer nano-templates.
Completed in year 3
10. Manipulation of molecules using electrical stimulation
Completed in year 3
11. Molecular dynamics simulations of structural and mechanical properties of oxide nanostructures and density functional theory studies of electronic properties of nano-wires and nano-ribbons.
Completed in year 3
12. Development and testing of amorphous magnetic ribbons for MI-based sensing.
Completed in year 5
13. Improving the field sensitivity and figure of merit of giant magnetoeimpedance (GMI) materials.
Initiated in year 4; currently underway.
14. CVD and cluster deposition of carbon nanotube networks.
Completed in year 1
15. Structural, electrical, and capacitive measurements on nanotube networks.
Completed in year 2
16. Biosensor fabrication using carbon nanotube arrays and evaluating the potential to sense different chemicals adsorbed to the surface.

*Investigation of gas sensors based on carbon nanotubes and biosensors based on functionalized magnetic nanoparticles using the have been completed and presented in this report. In addition to carbon nanotubes $\text{La}_{0.5}\text{Sr}_{0.5}\text{MnO}_3$ nanowires have also been investigated as a possible multifunctional sensor. Results were reported in 2011 annual report. **Complete***

17. Theoretical modeling and simulation of toxic absorption, external fields and mechanics on carbon nanotubes.

This milestone was dropped as the emphasis was shifted to experimental investigation of carbon nanotubes for biological and environmental sensor applications. (See 2011 annual report)

18. Magnetoimpedance measurements and sensing of biomolecules.

Ongoing

19. Integrated ferroelectric-ferromagnetic high-aspect ratio nanostructures

Ongoing

20. Magnetic nanoparticle attachment to cell membranes.

Completed in year 1

21. Design and fabrication of lithographically patterned metallic micro wires.

Completed in year 2

22. Design and fabrication of substrates with controlled nanotopography.

Discontinued as initial results were not promising.

23. Study of cell migration, cell-substrate adhesion, and cell growth.

Merged with the project to develop an artificial Matrigel.

24. Stimuli-response studies using ECIS of magnetic nanoparticle loaded cells.

Merged with the project to develop an artificial Matrigel.

25. An integrated functional materials approach to the development of an artificial Matrigel.

*Results presented in 2010, 2011 annual reports. **Complete.***

26. Formation and delivery of functionalized artificial platelets for rapid cessation of internal bleeding.

Ongoing

27. Chemical synthesis of ferrite nanoparticles and fabrication of polymer nanocomposite films, analysis of structural, electrical and magnetic properties.

Completed in year 3

28. PLD growth of ferroelectric/ferrite heterostructures with controlled interface strain, RF and microwave measurements of polymer composites and oxide films.

Completed in year 3

29. Materials growth efforts continued with piezoelectric films containing nanoparticle inclusions, experiments to study the magneto-electric and multiferroic coupled response in materials and prototype device structures.

Ongoing

30. Fabricate and characterize $\text{ZnO}:\text{V}$, $\text{ZnO}:\text{Mn}$ and $\text{ZnO}:\text{V}/\text{ZnO}:\text{Mn}$ heterostructures. Investigate the multiferroic coupling in these structures.

Completed in year 4

31. Synthesis of ferroelectric-ferromagnetic nanopillar-nanoparticle structure and exploration of magnetoelectric coupling.

Ongoing

32. Synthesis and characterization of PbSe and PbS_xSe_{1-x} nanoparticles by microwave plasma.

Completed in year 2

33. Integration of nanoparticles with polymer and characterization of optical properties.

Completed in year 4

34. Formation of single cell device structures with nanoparticles of different sizes and characterization of the output.

Completed in year 4

35. Fabrication and evaluation of tandem structures.

36. Synthesis and characterization of InSb nanoparticles.

37. Fabricate InSb-polymer hybrid solar cell structures and compare the performance with PbSe based devices

Synthesis of InSb quantum dots has not been successful. PbSe quantum dots are still the most efficient material for solar absorption to generate excitons. We have combined the tasks 35, 36, and 37 to investigate multi exciton generation and dissociation in PbSe QD by a femtosecond pump-probe technique. This study is underway.

38. Bulk nanocomposites: optimize synthesis parameters.

Completed in year 2

39. Core-shell approach towards optimization.

Completed in year 2

40. Structural and calorimetric analysis for thermal stability tests.

Completed in year 3

41. Measurement of TE properties.

Completed in year 5

42. Comparative studies and analysis: Synthesis bulk materials for comparison to the nano-scale TE materials.

Completed in year 4

43. Optimization employing the developed materials.

Completed in year 5

44. Device design development.

Ongoing

45. Measurement, optimization and re-development of prototype TE devices.

Ongoing

46. Theoretical modeling of conductance and thermopower of core-shell nanocomposites.

Completed in year 3

47. Fabrication of CaCoO nanoparticle coatings by a microwave plasma process and investigation of thermoelectric properties.

Completed in year 4

48. Synthesis of bulk thermoelectric.

Completed in year 5

Ongoing Milestones:

TASK I

1. Synthesis of PEG, Dextran coated nanoparticles and clusters for hyperthermia experiments and their structural and magnetic characterization.
2. Measurements and comparative analysis of specific absorption rates and AC power losses of ferrofluids for magnetic hyperthermia applications.
3. Improving the field sensitivity and figure of merit of giant magnetoimpedance (GMI) materials.
4. Magnetoimpedance measurements and sensing of biomolecules.
5. Integrated ferroelectric-ferromagnetic high-aspect ratio nanostructures
6. Formation and delivery of functionalized artificial platelets for rapid cessation of internal bleeding.

TASK II

7. Materials growth efforts continued with piezoelectric films containing nanoparticle inclusions, experiments to study the magneto-electric and multiferroic coupled response in materials and prototype device structures.
8. Synthesis of ferroelectric-ferromagnetic nanopillar-nanoparticle structure and exploration of magnetoelectric coupling.
9. Investigation of multi-exciton generation and dissociation in PbSe QD by a femtosecond pump-probe technique. This study is under way.

TASK III

10. Device design development.
11. Measurement, optimization and re-development of prototype TE devices.

Project Milestones for Continuation Proposal:

We received funding for continuation of this project for another three-year period till 9/19/2013. The following tables identify the milestones and timeline for each of the seven projects in the continuing proposal. The additional work is italicized and the revised timelines (for each project) are indicated. Green bars indicate accomplished work while the yellow bars indicate tasks that have been changed or merged based on the results. This rearrangement is based on the considerations described in the update on milestones:

Task I: Nanostructured materials for biomedical diagnostics and chemical sensing

Project 1: Functional magnetic fluids for biomedical applications.

| RESEARCH TASKS | Year 1 | Year 2 | Year 3 | Year 4 | Year 5 | Year 6 |
|---|--------|--------|--------|--------|--------|--------|
| Chemical synthesis of magnetic nanoparticles and ferrofluids, Structural analysis, DC and AC magnetization studies | | | | | | |
| Functionalization of ferrofluids with biocompatible surfactant coatings of the nanoparticles. Chemical and Physical properties characterization of the functionalized ferrofluids | | | | | | |
| Studies of magnetic and hydrodynamic properties of bio-functionalized ferrofluids under flow conditions | | | | | | |
| <i>Synthesis of PEG, Dextran coated nanoparticles and clusters for hyperthermia experiments and their structural and magnetic characterization</i> | | | | | | |
| <i>Measurements and comparative analysis of specific absorption rates and AC power losses of ferrofluids for magnetic hyperthermia applications</i> | | | | | | |
| <i>Bifunctional metal-oxide coupled and core-shell nanostructures</i> | | | | | | |

Project 2: Nanoparticle/nano-wire structures and polymer nanoparticles for sensing and molecular manipulation

| RESEARCH TASKS | Year 1 | Year 2 | Year 3 | Year 4 | Year 5 | Year 6 |
|--|--------|--------|--------|--------|--------|--------|
| Synthesis and characterization of Au templates with variable spacing and formation of In nano-pore structures | | | | | | |
| Growth of nano-wires of inorganic compounds with variable diameters. | | | | | | |
| Formation of polymer nano-templates | | | | | | |
| Manipulation of molecules using electrical stimulation | | | | | | |
| Molecular dynamics simulations of structural and mechanical properties of oxide nanostructures and density functional theory studies of electronic | | | | | | |

| | | | | | | | |
|--|--|--|--|--|--|--|--|
| properties of nano-wires and nano-ribbons | | | | | | | |
| <i>Development and testing of amorphous magnetic ribbons for MI-based sensing</i> | | | | | | | |
| <i>Improving the field sensitivity and figure of merit of giant magnetoimpedance (GMI) materials</i> | | | | | | | |

Project 3: Carbon-nanotube based sensors

| RESEARCH TASKS | Year 1 | Year 2 | Year 3 | Year 4 | Year 5 | Year 6 |
|---|--------|--------|--------|--------|--------|--------|
| CVD and cluster deposition of carbon nanotube networks | | | | | | |
| Structural, electrical, and capacitive measurements on nanotube networks | | | | | | |
| Biosensor fabrication using carbon nanotube arrays and evaluating the potential to sense different analytes adsorbed to the surface | | | | | | |
| Theoretical modeling and simulation of toxic absorption, external fields and mechanics on carbon nanotubes | | | | | | |
| <i>Magnetoimpedance measurements and sensing of biomolecules</i> | | | | | | |
| <i>Integrated ferroelectric-ferromagnetic high-aspect ratio nanostructures</i> | | | | | | |

Project 4: Functional materials for affecting cell proliferation and locomotion

| RESEARCH TASKS | Year 1 | Year 2 | Year 3 | Year 4 | Year 5 | Year 6 |
|---|--------|--------|--------|--------|--------|--------|
| Magnetic nanoparticle attachment to cell membranes | | | | | | |
| Design and fabrication of lithographically patterned metallic micro wires | | | | | | |
| Design and fabrication of substrates with controlled nanotopography | | | | | | |
| Study of cell migration, cell-substrate adhesion, and cell growth | | | | | | |
| <i>Stimuli-response studies using ECIS of magnetic nanoparticle loaded cells</i> | | | | | | |
| <i>An integrated functional materials approach to the development of an artificial Matrigel</i> | | | | | | |
| <i>Formation and delivery of functionalized artificial platelets for rapid cessation of internal bleeding</i> | | | | | | |

Task II: Multifunctional composites for communication and energy applications

Project 5: Tunable multifunctional nano- and heterostructures for RF and microwave applications

| RESEARCH TASKS | Year 1 | Year 2 | Year 3 | Year 4 | Year 5 | Year 6 |
|--|--------|--------|--------|--------|--------|--------|
| Chemical synthesis of ferrite nanoparticles and fabrication of polymer nanocomposite films, analysis of structural, electrical and magnetic properties | | | | | | |
| PLD growth of ferroelectric/ferrite heterostructures with controlled interface strain, RF and microwave measurements of polymer composites and oxide films | | | | | | |
| Materials growth efforts continued with piezoelectric films containing nanoparticle inclusions, experiments to study the magneto-electric and multiferroic coupled response in materials and prototype device structures | | | | | | |
| <i>Fabricate and characterize ZnO:V, ZnO:Mn and ZnO:V/ZnO:Mn heterostructures. Investigate the multiferroic coupling in these structures</i> | | | | | | |
| <i>Synthesis of ferroelectric-ferromagnetic nanopillar-nanoparticle structure and exploration of magnetoelectric coupling.</i> | | | | | | |

Project 6: Flexible photonic materials for solar-based energy sources

| RESEARCH TASKS | Year 1 | Year 2 | Year 3 | Year 4 | Year 5 |
|---|--------|--------|--------|--------|--------|
| Synthesis and characterization of PbSe and PbS _x Se _{1-x} nanoparticles by microwave plasma | | | | | |
| Integration of nanoparticles with polymer and characterization of optical properties | | | | | |
| Formation of single cell device structures with nanoparticles of different sizes and characterization of the output | | | | | |
| Fabrication and evaluation of tandem structures | | | | | |
| Synthesis and characterization of InSb nanoparticles | | | | | |
| Fabricate InSb-polymer hybrid solar cell structures and compare the performance with PbSe based devices | | | | | |

Task III: Solid-state materials for power generation and refrigeration

Project 7: High-performance bulk and nanocomposite thermoelectric materials for power generation

| RESEARCH TASKS | Year 1 | Year 2 | Year 3 | Year 4 | Year 5 | Year 6 |
|--|--------|--------|--------|--------|--------|--------|
| Bulk nanocomposites: optimize synthesis parameters | | | | | | |
| Core-shell approach towards optimization | | | | | | |
| Structural and calorimetric analysis for thermal stability tests | | | | | | |
| Measurement of TE properties | | | | | | |
| Comparative studies and analysis: Synthesis bulk materials for comparison to the nano-scale TE materials | | | | | | |
| Optimization employing the developed materials | | | | | | |
| Device design development | | | | | | |
| Measurement, optimization and re-development of prototype TE devices | | | | | | |
| Theoretical modeling of conductance and thermopower of core-shell nanocomposites | | | | | | |
| <i>Fabrication of CaCoO nanoparticle coatings by a microwave plasma process and investigation of thermoelectric properties</i> | | | | | | |
| <i>Synthesis of bulk thermoelectrics</i> | | | | | | |

V. Bibliography

1. Q A Pankhurst, J Connolly, S K Jones and J Dobson, *J. Phys. D: Appl. Phys.* **36** , R167-R181 (2003).
2. K. M. Kannan, *IEEE Trans. Magn.* **46**, 2523 (2010)
3. C G Hadjipanayis, M J Bonder, S Balakrishnan, X Wang, H Mao, and G C Hadjipanayis, *Small* **4**, 1925 (2008).
4. G. S. Chaubey, C. Barcena, N. Poudyal, C. Rong, J. Gao, S. Sun and J. P Liu *J. Am. Chem. Soc.* **129**, 7214-7215(2007).
5. H. Khurshid, V. Tzitzios, W. Li, C. G. Hadjipanayis and G. C. Hadjipanayis *J. Appl Phys.* **107**, 09A333 (2010).
6. C. B. Murray and C. R. Kagan and M. G. Bawendi *Annu. Rev. Mater. Sci.* **30**, 545–610 (2000).
7. S. Gangopadhyay, G. C. Hadjipanayis, C. M. Sorensen, K. J. Klabunde, V. Papaefthymiou, A. Kostikas, *Phys. Rev. B* **45** (1992) 9778.
8. T. K. Jain, M. a. Morales, S. K. Sahoo, D. L. Leslie-Pelecky and V. Labhasetwar, *Molecular Pharmaceutics* **2**, 194 (2005).
9. Redl, F. X.; Black, C. T.; Papaefthymiou, G. C.; Sandstrom, R. L.; Yin, M.; Zeng, H.; Murray, C. B.; O'Brien, S. P. *Journal of the American Chemical Society* 2004, 126.
10. Vonhoene, J.; Charles, R. G.; Hickam, W. M, *Journal of Physical Chemistry* 1958, 62, 1098-1101.
11. Ung, D.; Tung, L. D.; Caruntu, G.; Delaportas, D.; Alexandrou, I.; Prior, I. A.; Thanh, N. T. K., Variant shape growth of nanoparticles of metallic Fe-Pt, Fe-Pd and Fe-Pt-Pd alloys. *Crystengcomm* 2009, 11
12. H. Khurshid, V. Tzitzios, W. Li, C. G. Hadjipanayis, and G. C. Hadjipanayis, *Journal of Applied Physics* **107** (2010).
13. S. Karmakar, S. Taran, E. Bose, and B. K. Chaudhuri, *Phys. Rev. B.* **77** (2008).
14. X. Chen, S. Bedanta, O. Petravic, W. Kleemann, S. Sahoo, S. Cardoso, and P. P. Freitas, *Physical Review B* **72** (2005).
15. K. Binder and A. P. Young, *Physical Review B* **29**, 2864 (1984).
16. C. Djurberg, P. Svedlindh, P. Nordblad, M. F. Hansen, F. Bodker, and S. Morup, *Physical Review Letters* **79**, 5154 (1997).
17. C. Morales, J. Dewdney, S. Susmita, S. Skidmore, K. Stojak, H. Srikanth, T. Weller and J. Wang, *IEEE Trans. Magn.* **1**, 1340 (2010).
18. K. Stojak, S. Pal, H. Srikanth, C. Morales, J. Dewdney, J. Wang, T. Weller, *Nanotech.* **22**, 135602 (2011).
19. S. Pal, S. Chandra, M.H. Phan, P. Mukherjee, and H. Srikanth, *Nanotech.* **20**, 485604 (2009).
20. M. H. Phan and H.X. Peng, *Prog. Mater. Sci.* **53**, 323 (2008).
21. C. Garcia, V. Zhukova, A. Zhukov, N. Usov, M. Ipatov, J. Gonzalez and J. M. blanco, *Sensors Letters* **5**, 1 (2007).
22. H. Chiriac, D.D. Herea, S. Corodeanu, *J. Magn. Mater.* **311**, 425 (2007).
23. V.S. Larin, A.V. Torcunov, A. Zhukov, J. Gonzalez, M. Vazquez, L. Panina, *J. Magn. Mater.* **249**, 39 (2002).
24. C. L. Weston, M.J. Glantz, and J.R. Connor, *Fluids Barriers of the CNS* **8**, 14 (2011).
25. S. X. Wang and G. X. Li, *IEEE Trans. Magn.* **44**, 1687 (2008).

26. G. V. Kurlyandskaya, V. Fal Miyar, A. Saad, E. Asua, and J. Rodriguez, *J. Appl. Phys* **101**, 054505 (2007).
27. D. Mukherjee, N. Bingham, M. H. Phan, H. Srikanth, P. Mukherjee, and S. Witanachchi, "Ziz-zag Interface and Strain-influenced Ferromagnetism in Epitaxial $\text{Mn}_3\text{O}_4/\text{La}_{0.7}\text{Sr}_{0.3}\text{MnO}_3$ Thin Films grown on SrTiO_3 (100) substrates", *J. Appl. Phys.* (accepted for publication in April, 2012, issue).
28. C. A. F. Vaz, Y. Segal, J. Hoffman, R. D. Grober, F. J. Walker, and C. H. Ahn, *Appl. Phys. Lett.* **97**, 042506 (2010).
29. S. Dussan, A. Kumar, J. F. Scott, and R. S. Katiyar, *Appl. Phys. Lett.* **96**, 072904 (2010).
30. Y. G. Ma, W. N. Cheng, M. Ning, and C. K. Ong, *Appl. Phys. Lett.* **90**, 152911 (2007).
31. T. Wu, M. A. Zurbuchen, S. Saha, R. V. Wang, S. K. Streiffer, and J. F. Mitchell, *Phys. Rev. B* **73**, 134416 (2006).
32. M. A. Zurbuchen, T. Wu, S. Saha, J. Mitchell, S. K. Streiffer, *Appl. Phys. Lett.* **87**, 232908 (2005).
33. D. Mukherjee, R. Hyde, P. Mukherjee, H. Srikanth, and S. Witanachchi, *J. Appl. Phys.* **111**, 064102 (2012).
34. A. Pramanick, D. Damjanovic, J. E. Daniels, J. C. Nino, and J. L. Jones, *J. Am. Ceram. Soc.* **94**, 293-309 (2011)
35. V. N. Harshan and S. Kotru, *Integrated Ferroelectrics* **130**, 73–83 (2011).
36. A. Bentien, S. Johnsen, G. K. H. Madsen, B. B. Iversen, F. Steglich, *Euro. Phys. Lett.* **2007**, 80, 17008.
37. A. Bentien, G. K. H. Madsen, S. Johnsen, B. B. Iversen, *Phys. Rev. B* **2006**, 74, 205105.
38. P. Sun, M. Søndergaard, Y. Sun, S. Johnsen, B. B. Iversen, F. Steglich, *Appl. Phys. Lett.* **2011**, 98, 072105.
39. A. Herzog, M. Marutzky, J. Sichelschmidt, and F. Steglich, S. Kimura, S. Johnsen, B. B. Iversen, *Phys. Rev B* **2010**, 82, 245205.
40. A. -M. Racu, D. Menzel, J. Schoenes, M. Marutzky, S. Johnsen, B. B. Iversen, *J. App Phys.* **2008**, 103, 07C912.
41. Y. Zhang, M. S. Dresselhaus, Y. Shi, Z. F. Ren, G. Chen, *Nano Lett.* **2011**, 11, 1166.
42. I. A. Zaliznyak, A. T. Savici, V. O. Garlea, Rongwei Hu, C. Petrovic, *Phys. Rev. B* **2011**, 83, 184414.
43. A. K. L. Fan, G. H. Rosenthal, H. L. Mckinzie, A. Wold, *J. Solid State Chem.* **1972**, 5, 136.
44. A. A. Gippius, K.S. Okhotnikov, M. Baeritz, A. V. Shevelkov, *Solid State Phenomena* **2009**, 152, 287.
45. C. Petrovic, Y. Lee, T. Vogt, N. Dj. Lazarov, S. L. Bud'ko, P. C. Canfield, *Phys. Rev. B* **2005**, 72, 045103.
46. C. Petrovic, J. W. Kim, S. L. Bud'ko, A. I. Goldman, P. C. Canfield, W. Choe, G. J. Miller, *Phys. Rev. B* **2003**, 67, 155205.
47. S. Zhu, W. Xie, D. Thompson, T. Holgate, M. Zhou, Y. Yan, T. M. Tritt, *J. Mater. Res.* DOI:10.1557/jmr.2011.86.
48. J. Martin, G. S. Nolas, W. Zhang, L. Chen, *Appl. Phys. Lett.* **2007**, 90, 222112.

- 49. J. Martin, L. Wang, L. Chen, G. S. Nolas, *Phys. Rev. B* **2009**, 79, 115311.
- 50. A. Datta, J. Paul, A. Kar, A. Patra, Z. Sun, L. Chen, J. Martin, G. S. Nolas, *Cryst. Growth Design* **2010**, 10, 3983.
- 51. J. Xie, X. B. Zhao, J. L. Mi, J. Tu, H. Y. Qin, G. S. Cao, J. P. Tu, *Electrochem. Solid-State Lett.* **2006**, 9, A336.
- 52. L. Kumari, W. Li, J. Y. Huang, P. P. Provencio, *J. Phys. Chem. C* **2010**, 114, 9573.